A Schrödinger Cat Living in Two Boxes

Chen Wang,[1, *] Yvonne Y. Gao,[1] Philip Reinhold,[1] R. W. Heeres,[1] Nissim Ofek,[1] Kevin Chou,[1] Christopher Axline,[1] Matthew Reagor,[1] Jacob Blumoff,[1] K. M. Sliwa,[1] L. Frunzio,[1] S. M. Girvin,[1] Liang Jiang,[1] M. Mirrahimi,[1, 2] M. H. Devoret,[1] and R. J. Schoelkopf[1, †]

[1]*Department of Applied Physics and Physics, Yale University, New Haven, Connecticut 06511, USA*
[2]*INRIA Paris-Rocquencourt, Domaine de Voluceau, B. P. 105, 78153 Le Chesnay cedex, France*
(Dated: January 22, 2016)

Quantum superpositions of distinct coherent states in a single-mode harmonic oscillator, known as "cat states", have been an elegant demonstration of Schrödinger's famous cat paradox. Here, we realize a two-mode cat state of electromagnetic fields in two microwave cavities bridged by a superconducting artificial atom, which can also be viewed as an entangled pair of single-cavity cat states. We present full quantum state tomography of this complex cat state over a Hilbert space exceeding 100 dimensions via quantum non-demolition measurements of the joint photon number parity. The ability to manipulate such multi-cavity quantum states paves the way for logical operations between redundantly encoded qubits for fault-tolerant quantum computation and communication.

Rapid progress in controlling individual quantum systems over the past twenty years[1,2] has opened a wide range of possibilities of quantum information processing. Potential applications ranging from universal quantum computation to long-distance quantum communication share the central theme of exploiting quantum superpositions within a large Hilbert space. Further stimulated by curiosity about the quantum-classical boundary, there has been growing interest in generating superpositions of "macroscopically-distinguishable" states that are far apart in phase space. The canonical example is superpositions of coherent states of a harmonic oscillator, i.e. $\mathcal{N}(|\alpha\rangle + |-\alpha\rangle)$ with $\mathcal{N} \approx 1/\sqrt{2}$ at large $|\alpha|$, known as "cat states". The two components correspond to distinct quasi-classical wave-packets, in analogy to Schrödinger's *gedankenexperiment* of an unfortunate cat inside a closed box being simultaneously dead and alive. Cat states have so far been realized with single-mode optical[3] or microwave fields[1,4] with up to about 100 photons[5], but are increasingly susceptible to decoherence at large size.

Manipulating a large number of excitations in such harmonic oscillator states is one of two possible approaches to expand the information capacity of fully-controlled quantum systems. Cat states, which span a Hilbert space whose dimension grows linearly with the number of photons, are an attractive approach for redundantly encoding quantum information for error correction[6–8]. The other more traditional way to scale up a quantum system is to build many modes of excitations, each operated as a two-level qubit, so that the Hilbert space dimension increases exponentially with the number of modes[9,10]. Is it possible to combine the benefits of both approaches by creating a cat state that lives in more than a single mode or box? The idea of non-local or multi-mode cat dates back to the early days of cavity quantum electrodynamics (QED)[11], but experimental demonstration has remained a formidable challenge.

Here, we deterministically create a two-mode cat state of microwave fields in two superconducting cavities, using the strong dispersive interaction with a Josephson-junction-based artificial atom. This state can be expressed as:

$$|\psi_\pm\rangle = \mathcal{N}(|\alpha\rangle_A|\alpha\rangle_B \pm |-\alpha\rangle_A|-\alpha\rangle_B) \quad (1)$$

where $|\pm\alpha\rangle_A$ and $|\pm\alpha\rangle_B$ are coherent states of two microwave eigenmodes (Alice and Bob) at different frequencies, whose amplitudes are prepared equal for simplicity. Each of the two modes are predominantly localized in one of the two cavities that are weakly connected. Despite a nonzero (but small) spatial overlap of the two modes, we will refer for convenience to the state of each mode as the state of each cavity. Quantum superpositions of the form $|\psi_\pm\rangle$ have been previously realized in the optical domain[12] but were limited to small and non-orthogonal coherent states ($|\alpha|^2 = 0.65$). For larger $|\alpha|$ (*i.e.* $|\alpha|^2 \gtrsim 2$), $|\psi_\pm\rangle$ can be considered a single cat state living in two boxes whose superposed components are coherent states in a hybridized mode involving both Alice and Bob. Alternatively, in the more natural eigenmode basis, $|\psi_\pm\rangle$ has been known as the entangled coherent states in theoretical studies[13], and may also be understood as two single-cavity cat states that are entangled with each other.

The two-mode cat state is an eigenstate of the joint photon number parity operator P_J:

$$P_J = P_A P_B = e^{i\pi a^\dagger a} e^{i\pi b^\dagger b} \quad (2)$$

where $a(a^\dagger)$ and $b(b^\dagger)$ are the annihilation (creation) operators of photons in Alice and Bob, and P_A and P_B are the photon number parity operators in individual cavities. Remarkably, $|\psi_+\rangle$ (or $|\psi_-\rangle$) has definitively an even (or odd) number of photons in the two cavities combined, while the photon number parity in each cavity separately is maximally uncertain. Quantum non-demolition measurements of such parity operators not only illustrate the highly non-classical properties of the state, but also are instrumental for quantum error correction in general.

We realize measurements of the joint photon number parity and single-mode parities using the dispersive interaction with three energy levels of an artificial atom. Based on joint parity measurements, we further demonstrate full quantum state tomography of the two-cavity system[14]. This is obtained in the form of the joint Wigner function $W_J(\beta_A, \beta_B)$, which is a continuous-variable representation of the quantum state with β_A and β_B being complex variables in Alice and Bob respectively. Without correcting for the infidelity of the joint parity measurement operator, we observe quantum state fidelity of 81% for a two-mode cat state with $\alpha = 1.92$. The high-quality and high-dimensional quantum
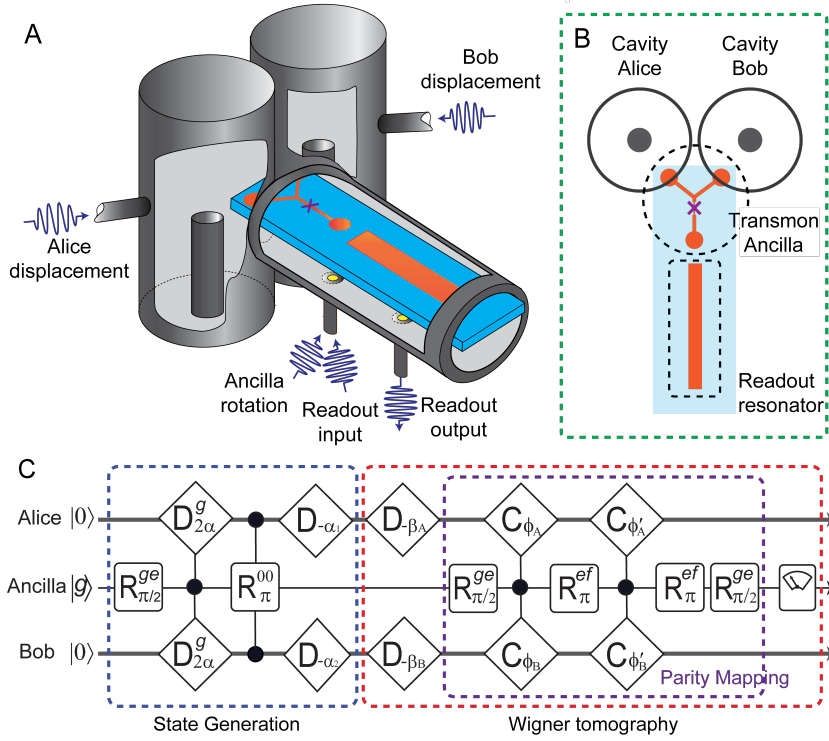
FIG. 1. **Sketch (not to scale) of device architecture and experimental protocol. (A)** A three dimensional schematic of the device consisting of two coaxial cavities (Alice and Bob), a Y-shaped transmon with a single Josephson junction (marked by "×"), and a stripline readout resonator. All components are housed inside a single piece of bulk high-purity aluminum, with artificial windows drawn for illustration purposes. **(B)** A top view of the same device, showing the relative position of the sapphire chip, center posts of the coaxial cavities, transmon antenna, and the readout resonator. **(C)** The microwave control sequences for generating the two-mode cat state and performing Wigner tomography. D_β represents cavity displacement by β, and a superscript g is added if the displacement is conditional on the ancilla being in $|g\rangle$. R_θ^{ge} or R_θ^{ef} represents ancilla rotation by angle θ (around an axis in the X-Y plane) in the $|g\rangle$-$|e\rangle$ Bloch sphere or $|e\rangle$-$|f\rangle$ Bloch sphere. R_π^{00} is an ancilla $|g\rangle$-$|e\rangle$ rotation conditional on the cavities being in $|0\rangle_A|0\rangle_B$. C_ϕ represents cavity phase shift of ϕ conditional on the ancilla being in an excited state. By choosing $\phi_i + \phi_i' = \pi$ or 2π, we can measure photon number parity of Alice (P_A), Bob (P_B), or the two combined (P_J), to perform Wigner tomography of individual cavities or the joint Wigner tomography.

control is further manifested by the presence of entanglement exceeding classical bounds in a CHSH-style inequality for two continuous-variable systems[14]. Finally, our two-cavity space effectively encodes two coupled logical qubits in the coherent state basis, and we present efficient two-qubit tomography in this encoded space.

Our experimental setup uses a three-dimensional (3D) circuit QED architecture[15], where two high-Q 3D cavities and a quasi-planar readout resonator simultaneously couple to a fixed-frequency transmon-type superconducting qubit (Fig. 1A,B)[16]. The two cavities that host the cat state of microwave photons are implementations of the longest-lived quantum memory in circuit QED to date[17]. The transmon, while usually considered a qubit, behaves as an artificial atom with multiple energy levels. We use the transmon as an ancilla to manipulate the multi-photon states in the two cavities, and its lowest three levels, $|g\rangle$, $|e\rangle$ and $|f\rangle$, are accessed in this experiment. The device is cooled down to 20 mK in a dilution refrigerator, and microwave transmission through the readout resonator is used to projectively measure the ancilla state with a heterodyne detection at room temperature after multiple stages of amplification.

We consider the Hamiltonian of the system including two harmonic cavity modes, a three-level atom, and their dispersive interaction (with parameters listed in Table I):

$$
\begin{aligned}
H/\hbar =&\, \omega_A a^\dagger a + \omega_B b^\dagger b + \omega_{ge}|e\rangle\langle e| + (\omega_{ge} + \omega_{ef})|f\rangle\langle f| \\
&- \chi_A^{ge} a^\dagger a|e\rangle\langle e| - (\chi_A^{ge} + \chi_A^{ef})a^\dagger a|f\rangle\langle f| \\
&- \chi_B^{ge} b^\dagger b|e\rangle\langle e| - (\chi_B^{ge} + \chi_B^{ef})b^\dagger b|f\rangle\langle f|
\end{aligned}
$$ (3)

where ω_A and ω_B are the angular frequencies of the two cavities (Alice and Bob), ω_{ge} and ω_{ef} are the $|e\rangle \to |g\rangle$ and $|f\rangle \to |e\rangle$ transition frequencies of the ancilla, χ_i^{ge} and χ_i^{ef}

($i = A$ or B) represent the dispersive frequency shifts of cavity i associated with the two ancilla transitions. The readout resonator and small high-order nonlinearities are neglected for simplicity. Using time-dependent external classical drives in the form of microwave pulses, we can perform arbitrary ancilla rotations in both $|g\rangle$-$|e\rangle$ and $|e\rangle$-$|f\rangle$ manifolds, and arbitrary cavity state displacements in Alice ($D_{\beta_A} = e^{\beta_A a^\dagger - \beta_A^* a}$) and Bob ($D_{\beta_B} = e^{\beta_B b^\dagger - \beta_B^* b}$) independently. More importantly, the state-dependent frequency shifts (χ's) allow cavity state manipulations conditioned on the ancilla level or vice versa using spectrally-selective control pulses, thus realizing atom-photon quantum logic gates[5]. It can be further shown that with separate drives on the two cavities and a drive on the ancilla, this Hamiltonian

		$\omega/2\pi$	T_1	T_2^*
Cavities:	Alice	4.2196612 GHz	2.2-3.3 ms	0.8-1.1 ms
	Bob	5.4467679 GHz	1.2-1.7 ms	0.6-0.8 ms
Transmon:	$|e\rangle \to |g\rangle$	4.87805 GHz	65-75 μs	30-45 μs
(Ancilla)	$|f\rangle \to |e\rangle$	4.76288 GHz	28-32 μs	12-24 μs

$\chi/2\pi$	Alice	Bob
χ^{ge}	0.71 MHz	1.41 MHz
χ^{ef}	1.54 MHz	0.93 MHz

TABLE I. Hamiltonian parameters and coherence times of the two storage cavities and the transmon ancilla, including transition frequencies ($\omega/2\pi$), dispersive shifts between each cavity and each transmon transition (χ), energy relaxation time (T_1), and Ramsey decoherence time (T_2^*). The cavity frequencies are given with a precision of ± 100 Hz and are stable over the course of several months.
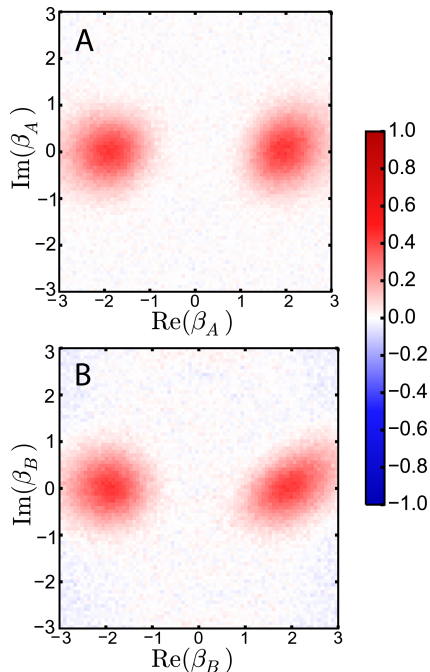
FIG. 2. **Wigner tomography of individual cavities.**
Measured single-cavity scaled Wigner function of **(A)** Alice
($\frac{\pi}{2}W_A(\beta_A)$) and **(B)** Bob ($\frac{\pi}{2}W_B(\beta_B)$) respectively for the two-
mode cats state $|\psi_-\rangle$, each plotted in the complex plane of
$\text{Re}(\beta_i)$ and $\text{Im}(\beta_i)$ (i=A or B). For either cavity, no interference
fringes are observed in its Wigner function, indicating a statisti-
cal mixture of two coherent states, as opposed to a single-cavity
cat state, after tracing out the quantum state of the other cav-
ity. The distortion of the coherent states is due to higher order
Hamiltonian terms (see supplementary). The photon number
parity within each cavity is close to 0, reflected by the value of
respective Wigner functions near the origin.

permits universal quantum control of the entire system[18].

We generate the two-mode cat state $|\psi_\pm\rangle$ deterministi-
cally using a series of logic gates as shown in Fig. 1C[19].
In particular, we implement effective displacements ($D_{2\alpha}^g$)
of both Alice and Bob conditional on ancilla being in
$|g\rangle$[16], which realizes a three-way entangling gate, $\frac{1}{\sqrt{2}}(|g\rangle +$
$|e\rangle)|0\rangle_A|0\rangle_B \rightarrow \mathcal{N}(|g\rangle|0\rangle_A|0\rangle_B + |e\rangle|2\alpha\rangle_A|2\alpha\rangle_B)$. Then
an ancilla rotation (R_π^{00}) conditional on the cavity state
$|0\rangle_A|0\rangle_B$ disentangles the ancilla, and subsequent cavity
displacements leave the cavities in a two-mode cat state.
The rotation axis controls the sign (or more generally, phase
angle) of the cat state superposition.

We probe the cat state by quantum non-demolition
(QND) measurements of the photon number parity. Parity
measurement of a single cavity using a dispersively coupled
ancilla qubit has been previously demonstrated[20,21], where
a conditional cavity phase shift[4], $C_\phi = \mathbb{I}\otimes|g\rangle\langle g| + e^{i\phi a^\dagger a}\otimes$
$|e\rangle\langle e|$, of $\phi = \pi$ allows the cavity states with even or odd
photon numbers to be mapped to $|g\rangle$ or $|e\rangle$ of the qubit
for subsequent readout. In our multi-cavity architecture,
measuring the joint photon number parity requires C_π in
both Alice and Bob, which is difficult to achieve simulta-
neously with existing techniques[21] unless $\chi_A^{ge} = \chi_B^{ge}$. We
overcome this challenge by exploiting the $|f\rangle$-level of the
transmon. By designing the frequency of the ancilla to
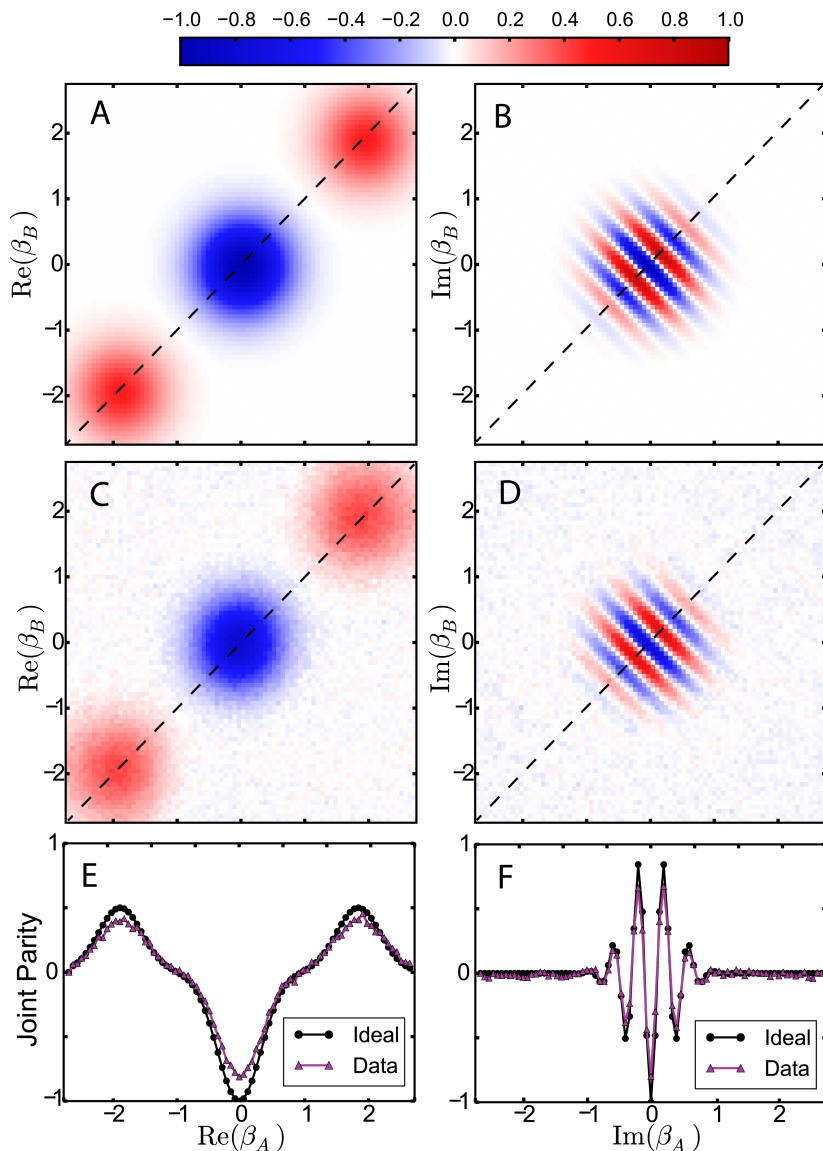be between those of the two cavities, the $|e\rangle \rightarrow |g\rangle$ tran-

sition shows stronger interaction with Bob ($\chi_B^{ge} > \chi_A^{ge}$),
while the $|f\rangle \rightarrow |e\rangle$ transition shows stronger interaction
with Alice ($\chi_A^{ef} > \chi_B^{ef}$). Manipulating the ancilla in differ-
ent superposition states among the three levels allows us
to concatenate conditional phase gates associated with χ_i^{ge}
and χ_i^{ef} with arbitrary weights[16]. This additional degree
of freedom not only allows for joint parity measurement
P_J (applying C_π to both cavities), but also enables parity
measurement of each cavity P_A or P_B individually without
affecting the other (applying C_π and $C_{2\pi}$ to the two cavities
respectively).

Based on single-cavity parity measurements, we can mea-
sure the Wigner function of individual cavities, $W_i(\beta_i) =$
$\frac{2}{\pi}Tr[\rho D_{\beta_i}P_i D_{\beta_i}^\dagger]$ (i=A or B)[20,22]. The Wigner function is
a standard method to fully determine the quantum state of
a single-continuous-variable system, which represents the
quasi-probability distribution of photons in the quadra-
ture space ($\text{Re}(\beta)$-$\text{Im}(\beta)$). Our measured W_A and W_B for
a two-mode cat state $|\psi_-\rangle$ with $\alpha = 1.92$ (Fig. 2) illus-
trates that the quantum state of either Alice or Bob on
its own is a statistical mixture of two clearly-separated co-
herent states with no coherence between them. In other
words, each cavity does not contain a regular (single-mode)
cat state, which would contain characteristic interference
fringes in the Wigner function[5,22] (and can also be straight-
forwardly generated in our experiment[16]). However, for a
state involving inter-cavity entanglement like $|\psi_-\rangle$, single-
cavity Wigner functions are insufficient for characterizing
the global quantum state. Such entanglement can be in-
ferred from measurement of the joint photon number par-
ity, $\langle P_J\rangle = -0.81 \pm 0.01$, even though each cavity alone
shows mean photon number parity of $\langle P_A\rangle \approx \langle P_B\rangle \approx 0$.
Additional evidence of the joint parity can be seen in a
spectroscopy measurement[16].

A full quantum state tomography of the two-cavity sys-
tem can be realized by measuring the joint Wigner func-
tion[23]:

$$W_J(\beta_A, \beta_B) = \frac{4}{\pi^2}\langle P_J(\beta_A, \beta_B)\rangle$$
$$= \frac{4}{\pi^2}Tr[\rho D_{\beta_A}D_{\beta_B}P_J D_{\beta_B}^\dagger D_{\beta_A}^\dagger] \qquad (4)$$

W_J is a function in the four-dimensional (4D) phase space,
whose value at each point ($\text{Re}(\beta_A)$, $\text{Im}(\beta_A)$, $\text{Re}(\beta_B)$,
$\text{Im}(\beta_B)$), after rescaling by $\pi^2/4$, is equal to the expec-
tation value of the joint parity after independent displace-
ments in Alice and Bob[14]. For simplicity, we will therefore
use the scaled joint Wigner function, or "displaced joint
parity" $\langle P_J(\beta_A, \beta_B)\rangle$ to represent the cavity state. $\langle P_J\rangle$ at
any given point (β_A, β_B) is directly measured by averaging
single-shot readout outcomes and takes values between -1
and +1. To illustrate the core features in this 4D Wigner
function of the state $|\psi_-\rangle$, we show its two-dimensional
(2D) cuts along the $\text{Re}(\beta_A)$-$\text{Re}(\beta_B)$ plane and $\text{Im}(\beta_A)$-
$\text{Im}(\beta_B)$ plane for both the calculated ideal state (Fig. 3A,
B, also see Ref. 14) and the measured data (Fig. 3C, D).
The Wigner function contains two positively-valued Gaus-
sian hyperspheres representing the probability distribution
of the two coherent-state components, and an interference
structure around the origin with strong negativity. Excel-
lent agreement is achieved between measurement and the-

FIG. 3. **Joint Wigner tomography.** **(A, B)** Two-dimensional plane-cut along (A) axes $\mathrm{Re}(\beta_A)$-$\mathrm{Re}(\beta_B)$ and (B) axes $\mathrm{Im}(\beta_A)$-$\mathrm{Im}(\beta_B)$ of the calculated 4D scaled joint Wigner function $\langle P_J(\beta_A, \beta_B)\rangle$ of the ideal odd-parity two-mode cat state $|\psi_-\rangle$ with $\alpha = 1.92$. The red features in (A) represent the probability distribution of the two coherent states components. The central blue feature in (A) and fringes in (B) demonstrate quantum interference between the two components. **(C, D)** The corresponding $\mathrm{Re}(\beta_A)$-$\mathrm{Re}(\beta_B)$ and $\mathrm{Im}(\beta_A)$-$\mathrm{Im}(\beta_B)$ plane-cuts of the measured joint Wigner function of $|\psi_-\rangle$, to be compared with the ideal results in (A) and (B) respectively. Data are taken in a 81×81 grid, where every point represents an average of about 2000 binary joint parity measurements. **(E)** Diagonal line-cuts of the data shown in (A) and (C), corresponding to 1D plots of the calculated (black) and measured (red) scaled joint Wigner function along $\mathrm{Re}(\beta_A) = \mathrm{Re}(\beta_B)$ with $\mathrm{Im}(\beta_A) = \mathrm{Im}(\beta_B) = 0$. **(F)** Diagonal line-cuts of the data shown in (B) and (D), corresponding to 1D plots of the calculated (black) and measured (red) scaled joint Wigner function along $\mathrm{Im}(\beta_A) = \mathrm{Im}(\beta_B)$ with $\mathrm{Re}(\beta_A) = \mathrm{Re}(\beta_B) = 0$.

ory, with the raw data showing an overall 81% contrast of the ideal Wigner function. Comprehensive measurements of $\langle P_J\rangle$ in the entire 4D parameter space further allow us to reconstruct the density matrix of the quantum state, which shows a total fidelity of also about 81% against the ideal $|\psi_-\rangle$ state. The actual state fidelity may be significantly higher if various errors associated with tomography are removed[16]. Additional visualization of the Wigner function data is presented in a Supplementary movie[16].

Analyzed within the energy eigen-mode basis (Alice and Bob), the two-mode cat state is a manifestation of quantum entanglement between two quasi-classical systems. The entanglement can be tested against a CHSH-style Bell's inequality constructed from displaced joint parity at 4 points in the phase space[14]. We measure a Bell signal[16] of 2.17 ± 0.01 for the state in Fig. 3, exceeding the classical bound of 2. Without complete spatial separation and fully independent readout of the two modes, the violation should be considered a demonstration of the fidelity of the entanglement and the measurement rather than a true test of non-locality. Nevertheless, various schemes exist to further separate the two modes such as converting the cavity fields

into itinerant microwave signals and/or optical photons[24].

Compared with other reported quantum states of two harmonic oscillators, a striking property of the two-mode cat state is that its underlying compositions are highly-distinguishable. Two-mode squeezed states[25–28] have shown strong entanglement, but are Gaussian states without the Wigner negativity and the phase space separation as in a cat state. The "$N00N$" state, an entangled state in the discrete Fock state basis, typically requires quantum operations of N photons one by one and so far has been realized with up to 5 photons[29,30]. The two components of the cat state in Fig. 3 have a phase space separation of $|\alpha - (-\alpha)| = \sqrt{15}$ in each cavity, giving an action distance of $\sqrt{30}$ in the 4D phase space, or a cat size[22] of 30 photons. Our technique in principle allows generation of two-mode cat states with arbitrary size using the same operation. So far we have measured cat sizes of up to 80 photons[16], and more macroscopic states can be achieved by implementing numerically optimized control pulses[31] and engineering more favorable Hamiltonian parameters.

Compared with single-cavity quantum states, the addition of the second cavity mode increases the quantum in-
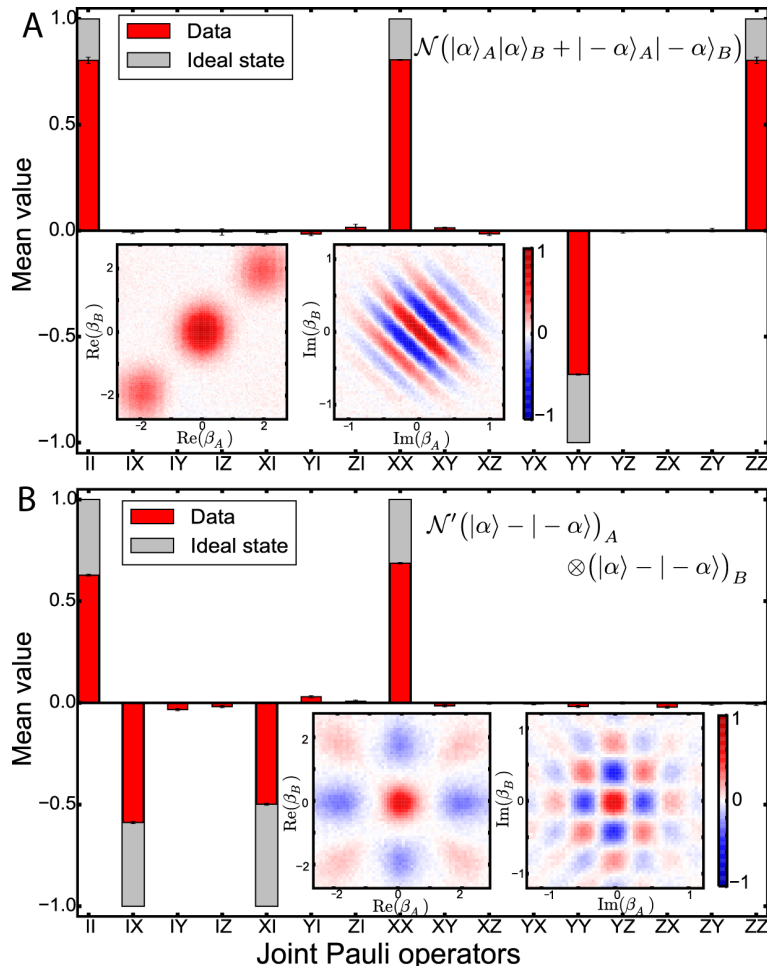
FIG. 4. **Encoded two-qubit tomography.** **(A)** Red bars show tomography of two logical qubits encoded in the coherent state basis of two cavities, with the prepared state being an even-parity two-mode cat state, $|\psi_+\rangle$ with $\alpha = 1.92$. Gray bars represent the ideal state. Insets show the $\text{Re}(\beta_A)$-$\text{Re}(\beta_B)$ and $\text{Im}(\beta_A)$-$\text{Im}(\beta_B)$ plane-cuts of the measured scaled joint Wigner function of the same state. The measured identity operator differs from 1 as a result of the parity measurement infidelity and leakage out of the code space. **(B)** Encoded two-qubit tomography of an approximate product state of single-cavity cat states, $\mathcal{N}'(|\alpha\rangle - |-\alpha\rangle)_A \otimes (|\alpha\rangle - |-\alpha\rangle)_B$ also with $\alpha = 1.92$. Insets show plane-cuts of the measured scaled joint Wigner function of the same state. Given familiarity with single-cavity cat states, these Wigner function patterns can be understood by considering $W_J(\beta_A, \beta_B) = W_A(\beta_A)W_B(\beta_B)$ for separable states. For example, the "checkerboard" patterns in the $\text{Im}(\beta_A)$-$\text{Im}(\beta_B)$ plane-cuts can be understood by multiplying orthogonal fringes from the two independent cat states.

formation capacity significantly. Despite the modest mean photon numbers, a full tomography of the two-mode cat state (partly shown in Fig. 3) requires a Hilbert space of at least 100 dimensions to be described (capturing 99% of the population), comparable to a 6 or 7 qubit GHZ state. Our conservatively estimated quantum state fidelity is comparable to that reported for an 8-qubit GHZ state in trapped ions[9] and the largest GHZ state in superconducting circuits[10] (5 qubits). In addition, a great advantage of continuous-variable quantum control is illustrated by our hardware-efficient quantum state tomography protocol that covers an enormous Hilbert space by simply varying two complex variables of cavity displacements.

An important motivation for creating multi-cavity cat states is to implement a promising paradigm towards fault-tolerant quantum computation[7,32], where information is redundantly encoded in the coherent state basis[5]. This approach has recently led to the first realization of quantum error correction of a logical qubit achieving the break-even point[8]. In this context, our experiment realizes an architecture of two coupled logical qubits. The two-mode cat state can be considered a two-qubit Bell state $\frac{1}{\sqrt{2}}(|0\rangle|0\rangle \pm |1\rangle|1\rangle)$, where the quasi-orthogonal coherent states $|\pm \alpha\rangle$ in each of the two cavities represent $|0\rangle$ and $|1\rangle$ of a logical qubit.

For any two-qubit logical state encoded in this subspace, we can perform efficient tomography without extensive measurement of the joint Wigner function. This is carried out by measuring $\langle P_J \rangle$ at 16 selected points of the phase

space (β_A, β_B)[16]. The encoded two-qubit tomography of a state $|\psi_+\rangle$ with $\alpha = 1.92$ is shown in Fig. 4A, providing a direct fidelity estimation[33] of $\frac{1}{4}(\langle II \rangle + \langle XX \rangle - \langle YY \rangle + \langle ZZ \rangle)$ $= 78\%$ against the ideal Bell state, surpassing the 50% bound for classical correlation. As a comparison, Fig. 4B illustrates a product state of single-mode cat states in Alice and Bob, which is identified as $|-X\rangle_A|-X\rangle_B$ in the logical space. For both states illustrated here, the two-qubit tomography suggests that errors within the encoded space are quite small. The reduced contrast compared to the ideal state is mostly due to infidelity of the joint parity measurement and leakage out of the code space (due to higher-order Hamiltonian terms).

In this Report, we have demonstrated a Schrödinger's cat that lives in two cavities. This two-mode cat state is not only a beautiful manifestation of mesoscopic superposition and entanglement constructed from quasi-classical states[13], but also a highly-desirable resource for quantum metrology[34], quantum networks and teleportation[35]. Moreover, the demonstration of high-fidelity quantum control over the large two-cavity Hilbert space has important implications for continuous-variable-based quantum computation. The measurement of the joint photon number parity realized here is QND by design, and will play a central role in quantum error correction[6,8,18] and facilitating concurrent remote entanglement[36] in a modular architecture of quantum computation.

* chen.wang@yale.edu

† robert.schoelkopf@yale.edu

[1] S. Haroche, Reviews of Modern Physics **85**, 1083 (2013).

[2] D. J. Wineland, Reviews of Modern Physics **85**, 1103 (2013).

[3] A. Ourjoumtsev, H. Jeong, R. Tualle-Brouri, and P. Grangier, Nature **448**, 784 (2007).

[4] M. Brune, E. Hagley, J. Dreyer, X. Matre, A. Maali, C. Wunderlich, J. M. Raimond, and S. Haroche, Physical Review Letters **77**, 4887 (1996).

[5] B. Vlastakis, G. Kirchmair, Z. Leghtas, S. E. Nigg, L. Frunzio, S. M. Girvin, M. Mirrahimi, M. H. Devoret, and R. J. Schoelkopf, Science **342**, 607 (2013).

[6] I. L. Chuang, D. W. Leung, and Y. Yamamoto, Physical Review A **56**, 1114 (1997).

[7] M. Mirrahimi, Z. Leghtas, V. V. Albert, S. Touzard, R. J. Schoelkopf, L. Jiang, and M. H. Devoret, New Journal of Physics **16**, 045014 (2014).

[8] N. Ofek, A. Petrenko, R. W. Heeres, P. Reinhold, Z. Leghtas, B. Vlastakis, Y. Liu, L. Frunzio, S. M. Girvin, L. Jiang, M. Mirrahimi, M. H. Devoret, and R. J. Schoelkopf, in preparation (2016).

[9] T. Monz, P. Schindler, J. T. Barreiro, M. Chwalla, D. Nigg, W. A. Coish, M. Harlander, W. Hnsel, M. Hennrich, and R. Blatt, Physical Review Letters **106**, 130506 (2011).

[10] J. Kelly, R. Barends, A. G. Fowler, A. Megrant, E. Jeffrey, T. C. White, D. Sank, J. Y. Mutus, B. Campbell, Y. Chen, Z. Chen, B. Chiaro, A. Dunsworth, I.-C. Hoi, C. Neill, P. J. J. OMalley, C. Quintana, P. Roushan, A. Vainsencher, J. Wenner, A. N. Cleland, and J. M. Martinis, Nature **519**, 66 (2015).

[11] L. Davidovich, A. Maali, M. Brune, J. M. Raimond, and S. Haroche, Physical Review Letters **71**, 2360 (1993).

[12] A. Ourjoumtsev, F. Ferreyrol, R. Tualle-Brouri, and P. Grangier, Nature Physics **5**, 189 (2009).

[13] B. C. Sanders, Journal of Physics A: Mathematical and Theoretical **45**, 244002 (2012).

[14] P. Milman, A. Auffeves, F. Yamaguchi, M. Brune, J. M. Raimond, and S. Haroche, The European Physical Journal D - Atomic, Molecular, Optical and Plasma Physics **32**, 233 (2005).

[15] H. Paik, D. I. Schuster, L. S. Bishop, G. Kirchmair, G. Catelani, A. P. Sears, B. R. Johnson, M. J. Reagor, L. Frunzio, L. I. Glazman, S. M. Girvin, M. H. Devoret, and R. J. Schoelkopf, Physical Review Letters **107**, 240501 (2011).

[16] See, Supplementary materials for additional information.

[17] M. Reagor, W. Pfaff, C. Axline, R. W. Heeres, N. Ofek, K. Sliwa, E. Holland, C. Wang, J. Blumoff, K. Chou, M. J. Hatridge, L. Frunzio, M. H. Devoret, L. Jiang, and R. J. Schoelkopf, arXiv:1508.05882 [cond-mat, physics:quant-ph] (2015).

[18] M. Michael, M. Silveri, R. T. Brierley, V. V. Albert, J. Salmilehto, L. Jiang, and S. M. Girvin, in preparation (2016).

[19] Z. Leghtas, G. Kirchmair, B. Vlastakis, M. H. Devoret, R. J. Schoelkopf, and M. Mirrahimi, Physical Review A **87**, 042315 (2013).

[20] P. Bertet, A. Auffeves, P. Maioli, S. Osnaghi, T. Meunier, M. Brune, J. M. Raimond, and S. Haroche, Physical Review Letters **89**, 200402 (2002).

[21] L. Sun, A. Petrenko, Z. Leghtas, B. Vlastakis, G. Kirchmair, K. M. Sliwa, A. Narla, M. Hatridge, S. Shankar, J. Blumoff, L. Frunzio, M. Mirrahimi, M. H. Devoret, and R. J. Schoelkopf, Nature **511**, 444 (2014).

[22] S. Delglise, I. Dotsenko, C. Sayrin, J. Bernu, M. Brune, J.-M. Raimond, and S. Haroche, Nature **455**, 510 (2008).

[23] K. E. Cahill and R. J. Glauber, Physical Review **177**, 1882 (1969).

[24] R. W. Andrews, A. P. Reed, K. Cicak, J. D. Teufel, and K. W. Lehnert, Nature Communications **6**, 10021 (2015).

[25] Z. Y. Ou, S. F. Pereira, H. J. Kimble, and K. C. Peng, Physical Review Letters **68**, 3663 (1992).

[26] B. Julsgaard, A. Kozhekin, and E. S. Polzik, Nature **413**, 400 (2001).

[27] C. Eichler, D. Bozyigit, C. Lang, M. Baur, L. Steffen, J. M. Fink, S. Filipp, and A. Wallraff, Physical Review Letters **107**, 113601 (2011).

[28] E. Flurin, N. Roch, F. Mallet, M. H. Devoret, and B. Huard, Physical Review Letters **109**, 183901 (2012).

[29] I. Afek, O. Ambar, and Y. Silberberg, Science **328**, 879 (2010).

[30] H. Wang, M. Mariantoni, R. C. Bialczak, M. Lenander, E. Lucero, M. Neeley, A. D. OConnell, D. Sank, M. Weides, J. Wenner, T. Yamamoto, Y. Yin, J. Zhao, J. M. Martinis, and A. N. Cleland, Physical Review Letters **106**, 060401 (2011).

[31] N. Khaneja, T. Reiss, C. Kehlet, T. Schulte-Herbrggen, and S. J. Glaser, Journal of Magnetic Resonance **172**, 296 (2005).

[32] P. T. Cochrane, G. J. Milburn, and W. J. Munro, Physical Review A **59**, 2631 (1999).

[33] S. T. Flammia and Y.-K. Liu, Physical Review Letters **106**, 230501 (2011).

[34] J. Joo, W. J. Munro, and T. P. Spiller, Physical Review Letters **107**, 083601 (2011).

[35] S. J. van Enk and O. Hirota, Physical Review A **64**, 022313 (2001).

[36] A. Roy, L. Jiang, A. D. Stone, and M. Devoret, Physical Review Letters **115**, 150503 (2015).

Supplementary Material:
A Schrödinger Cat living in two boxes

Chen Wang,[1] Yvonne Y. Gao,[1] Philip Reinhold,[1] R. W. Heeres,[1] Nissim Ofek,[1] Kevin Chou,[1] Christopher Axline,[1] Matthew Reagor,[1] Jacob Blumoff,[1] K. M. Sliwa,[1] L. Frunzio,[1] S. M. Girvin,[1] Liang Jiang,[1] M. Mirrahimi,[1, 2] M. H. Devoret,[1] and R. J. Schoelkopf[1]

[1]*Department of Applied Physics and Physics, Yale University, New Haven, Connecticut 06511, USA*
[2]*INRIA Paris-Rocquencourt, Domaine de Voluceau, B. P. 105, 78153 Le Chesnay cedex, France*
(Dated: January 22, 2016)

MATERIALS AND METHODS

A. Device Architecture

Our cQED system includes two 3D cavities, a quasi-planar linear resonator, and a Y-shaped transmon. A single block of high-purity (5N5) aluminum is machined to form a 3D structure that contains both superconducting cavity resonators and also functions as a package for the sapphire chip with deposited Josephson junction. Each of the two cavities can be considered a 3D version of a $\lambda/4$ transmission line resonator between a center stub 3.2 mm in diameter and a cylindrical wall (outer conductor) 9.5 mm in diameter[1]. The heights of the stubs control the resonance frequency, and are about 12.2 mm and 16.3 mm respectively for Alice and Bob. A tunnel (with a maximum width of 5.8 mm and a maximum height of 3.9 mm) is opened from the outside towards the middle wall between the two cavities, creating a three way joint between the tunnel and the two cavities (see photo image, Fig. S1). The whole package is chemically etched by about 80 μm after machining to improve the surface quality of the cavity resonators[2].

The superconducting transmon is on a 5.5 mm × 27.5 mm chip, which is diced from a 430 μm-thick c-plane sapphire wafer after fabrication. The fabrication process uses electron-beam lithography and the standard shadow-mask evaporation of Al/AlOx/Al Josephson junction. The sapphire chip is inserted into the tunnel, with the antenna pads of the transmon slightly intruding into the coaxial cavities to provide mode coupling. The chip is mechanically held at one end with an aluminum clamping structure and indium seal[3].

During the transmon fabrication process, a 100 μm×9.8 mm strip of aluminum film is also deposited on the sapphire chip. This metal strip and the wall of the tunnel form a planar-3D hybrid $\lambda/2$ stripline resonator. This resonator design has the advantages of both lithographic dimensional control and low surface/radiation loss, and is systematically studied in Ref. 3. Here it is capacitively coupled to the transmon, and strongly coupled to a 50 Ω transmission line for readout.

B. Sytem Hamiltonian Model

The cQED system has four bosonic modes involved in this experiment: the two 3D cavities, the readout resonator and the transmon ancilla. The transmon can be understood as an LC oscillator with much larger anharmonic-
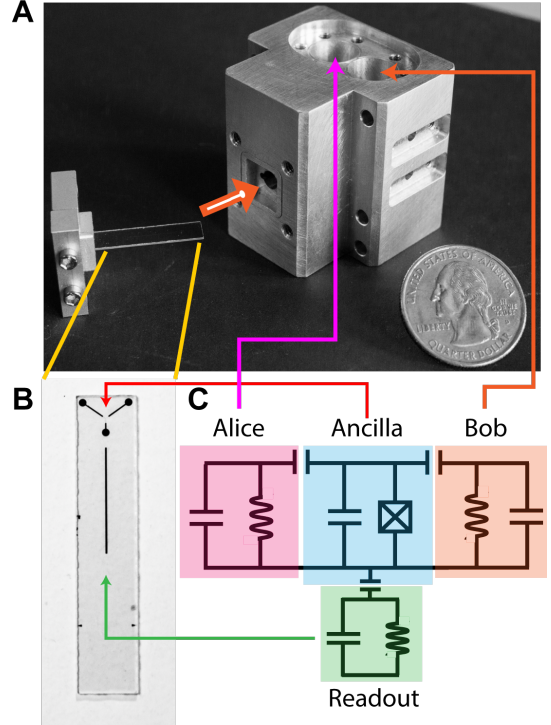

FIG. S1. **Overview of the 3D cQED device. (A)** A photograph of the full assembly of the device used for this study. The machined aluminum package contains two coaxial stub cavity resonators. A sapphire chip hosting the transmon ancilla, clamped by an aluminum chip-holder, is inserted through a tunnel to be coupled to the two cavities from the side. The sapphire chip contains an extra strip of aluminum, forming a stripline resonator with the tunnel wall. **(B)** A micrograph image of the Y-shaped transmon. **(C)** A schematic effective circuit of the cQED system containing three LC oscillators and one anharmonic oscillator (artificial atom) coupled together.

ity compared with the other modes, and is treated explicitly as a three-level artificial atom. Following Black-box quantization of superconducting circuits[4], the other cavity/resonator modes are modeled as near-harmonic oscillators with weak nonlinearity inherited from coupling to the Josephson junction.

The full system Hamiltonian can then be written in the following form up to the fourth order in the coupling of the

resonators to the transmon:

$$
\begin{aligned}
H/\hbar =\ & \omega_A(a^\dagger a + \tfrac{1}{2}) + \omega_B(b^\dagger b + + \tfrac{1}{2}) + \omega_R(r^\dagger r + \tfrac{1}{2}) \\
& + \omega_{ge}|e\rangle\langle e| + (\omega_{ge} + \omega_{ef})|f\rangle\langle f| \\
& - \chi_A^{ge} a^\dagger a |e\rangle\langle e| - (\chi_A^{ge} + \chi_A^{ef}) a^\dagger a |f\rangle\langle f| \\
& - \chi_B^{ge} b^\dagger b |e\rangle\langle e| - (\chi_B^{ge} + \chi_B^{ef}) b^\dagger b |f\rangle\langle f| \\
& - \chi_R^{ge} r^\dagger r |e\rangle\langle e| - (\chi_R^{ge} + \chi_R^{ef}) r^\dagger r |f\rangle\langle f| \\
& - \frac{K_A}{2} a^\dagger a^\dagger aa - \frac{K_B}{2} b^\dagger b^\dagger bb - \frac{K_R}{2} r^\dagger r^\dagger rr \\
& - K_{AB} a^\dagger a b^\dagger b - K_{AR} a^\dagger a r^\dagger r - K_{BR} b^\dagger b r^\dagger r \qquad \text{(S1)}
\end{aligned}
$$

Eq. (S1) is an expanded version of Eq. (3) of the main text, which now includes the readout resonator (with subscript R and operators r and $r^\dagger$) as well as Kerr nonlinearities of the cavities. The first two rows represent the excitation energy of the all modes, explicitly including the transmon anharmonicity of $\omega_{ge} - \omega_{ef} = 115.17$ MHz. The next three rows are second order terms (~ 1 MHz) representing the dispersive interactions (χ's) between the transmon and each of the three resonators. The last two rows are the fourth order terms (~ 10 kHz), including the self-Kerr energies (K_A, K_B, K_R) of the resonators and the cross-Kerr interactions between any pairs of resonators (K_{AB}, K_{AR}, K_{BR}). All Hamiltonian parameters of our device are listed in Table S1.

The key Hamiltonian terms that enable the cat state generation and joint parity measurement are the dispersive shifts, $\chi_A^{ge}, \chi_A^{ef}, \chi_B^{ge}, \chi_B^{ef}$, highlighted in the main text. Since the readout resonator is always kept in the vacuum state until a final measurement is needed, its Hamiltonian terms do not affect the quantum control and quantum state evolution in this experiment. The fourth-order Hamiltonian terms of Alice and Bob give a minor contribution to the infidelity of the experiment. The self-Kerr terms (K_A and K_B) induce distortion of the Gaussian probability distribution of the coherent state components of the cat state, and will cause state collapse and revival at long time scales[5]. The cross-Kerr interaction K_{AB} induces spontaneous ent-Trueanglement between Alice and Bob over long time scales in ways not included in our simple analysis.

	Frequency $\omega/2\pi$	Nonlinear interactions versus: Alice	Bob	Readout
$|e\rangle \to |g\rangle$	4.87805 GHz	0.71 MHz	1.41 MHz	1.74 MHz
$|f\rangle \to |e\rangle$	4.76288 GHz	1.54 MHz	0.93 MHz	1.63 MHz
Alice	4.2196612 GHz	0.83 kHz	-9 kHz	5 kHz
Bob	5.4467677 GHz	-9 kHz	5.6 kHz	12 kHz
Readout	7.6970 GHz	5 kHz	12 kHz	7 kHz

TABLE S1. Hamiltonian parameters of all cQED components, including the transmon ancilla, the two cavity resonators (Alice and Bob) and the readout resonator. The measured parameters include all transition frequencies ($\omega/2\pi$), dispersive shifts between each resonator and each transmon transition ($\chi/2\pi$), the self-Kerr of Alice ($K_A/2\pi$) and Bob ($K_B/2\pi$), and the cross-Kerr interaction between Alice and Bob ($K_{AB}/2\pi$). The Kerr parameters and χ^{ef} associated with the readout resonator are theoretical estimates based on the other measured parameters.

C. Measurement Setup and Protocol

Fig. S2 shows the diagram of our measurement setup. The device package is installed inside a Cryoperm magnetic shield and thermalized to the mixing chamber of a dilution refrigerator with a base temperature of 20 mK. Low-pass filters and infrared (eccosorb) filters are used to reduce stray radiation and photon shot noise. A Josephson parametric converter (JPC) is also mounted to the 20 mK stage, connected to the output port of the device package via circulators, providing near-quantum-limited amplification, with a power gain of 20dB and bandwidth of 5MHz.

We use a field programmable gate array (FPGA) to operate both the quantum-control pulse sequences and the data acquisition process. Our experiment does not rely on the real-time feedback capability of the FPGA, but our in-house programmed FPGA offers an important practical advantage in its ability to compute rather than store sideband-modulation waveforms. This leads to minimal usage of waveform memory for a large number of different cavity displacements, allowing us to measure the joint Wigner function over a large number of points in the phase space in a single run.

Both cavity drives and transmon drives are generated by sideband-modulation of continuous-wave (CW) carrier tones produced by respective microwave generators. The 4 FPGA analogue channels are used as 2 IQ-pairs that control the cavity drives to implement arbitrary cavity displacements. Rotations of the transmon ancilla are controlled by another pair of IQ channels provided by an arbitrary waveform generator (AWG) synchronized to the FPGA via a digital marker. This IQ pair controls both $|g\rangle$-$|e\rangle$ and $|e\rangle$-$|f\rangle$ transitions by using different intermediate frequencies (IF).

Ancilla readout is performed by heterodyne measurement of the microwave transmission of a readout pulse through the two ports of the quasi-planar readout resonator near its resonance frequency. Using the well-established cQED dispersive readout[6], the amplitude and phase of the transmitted signal depends on the quantum state of the ancilla. This readout pulse is produced by a microwave generator (RO) gated by a FPGA digital channel. The transmitted signal, after being amplified by the JPC, is further amplified by a high electron mobility transistor (HEMT) at 4K and a regular RF amplifier at room temperature. The amplified signal is then mixed down to 50 MHz with the output of a "local oscillator" (LO) microwave generator, and analyzed by the FPGA. A split copy of the readout pulse is directly mixed with the LO without entering the refrigerator to provide a phase reference for the measured transmission.

The long lifetimes of the cavities allow preparation of highly coherent cavity quantum states, but severely limits the rate one can repeat the measurement process. (With $T_1 \approx 3$ ms for Alice, it takes 15-20 ms for the cavity photon number to naturally decay to the order of 0.01.) Since tomographic measurement of the two-cavity quantum state requires large amounts of measurements, we implement four-wave mixing processes to realize fast reset for both cavities[7]. These processes effectively convert photons in Alice or Bob into photons in the short-lived readout res-
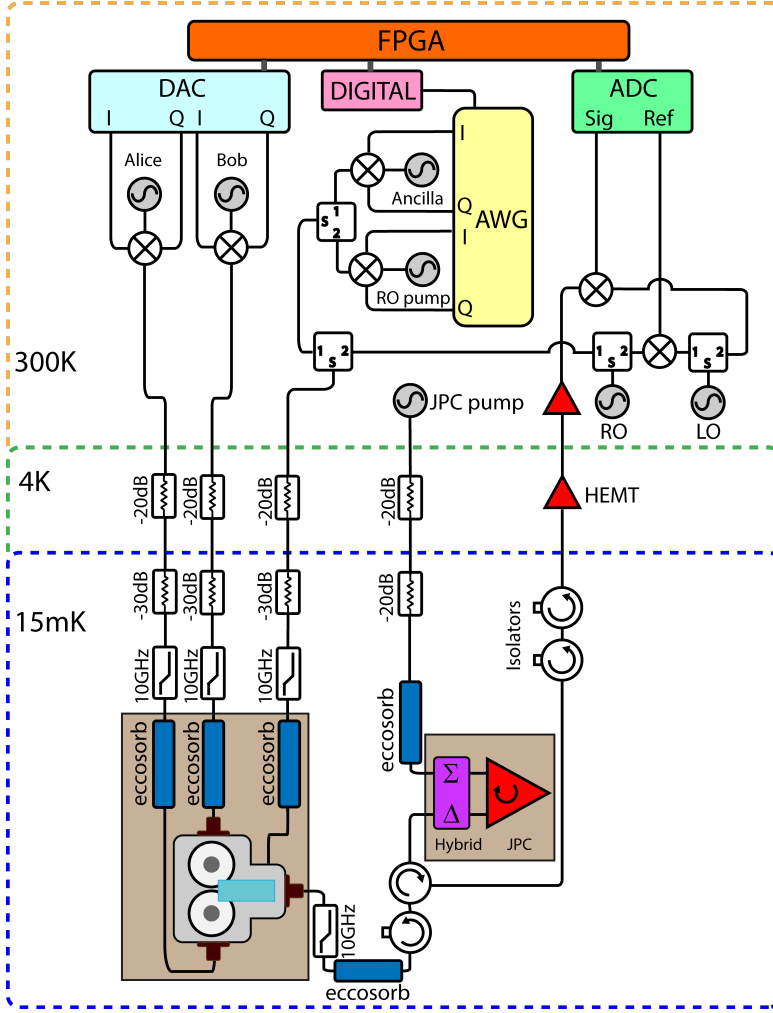
FIG. S2. **Circuit diagram of the measurement setup.** We use a field programmable gate array (FPGA) to control the experiment. The FPGA has a total of 4 analogue channels, which are used to provide I-Q control of the classical cavity drives via sideband modulation of the outputs of microwave generators labeled "Alice" and "Bob". These drives realize arbitrary cavity displacement operations D_α on the two high-Q cavities (Alice and Bob). A digital channel from the FPGA triggers an arbitrary waveform generator (AWG), whose two analogue channels provide I-Q control of the ancilla drives for both $|g\rangle - |e\rangle$ and $|e\rangle - |f\rangle$ rotation, modulating the microwave tone labeled "ancilla". The readout pulse is generated by a "RO" generator gated by a FPGA digital pulse, which is transmitted through the readout resonator for measuring the ancilla state. The transmitted signal is amplified by a Josephson parametric converter (JPC) at 15 mK, a high electron mobility transistor (HEMT) at 4K, a standard (Mini-circuit) RF amplifier at room temperature, and then mixed with a local oscillator ("LO") to produce a 50 MHz signal to be digitized and recorded by the FPGA. Another two analogue channels of the AWG controls an off-resonant pump on the readout resonator ("RO pump"). This drive, together with off-resonant pumps on Alice and Bob, allows fast reset of the high-Q cavities through 4-wave mixing processes.
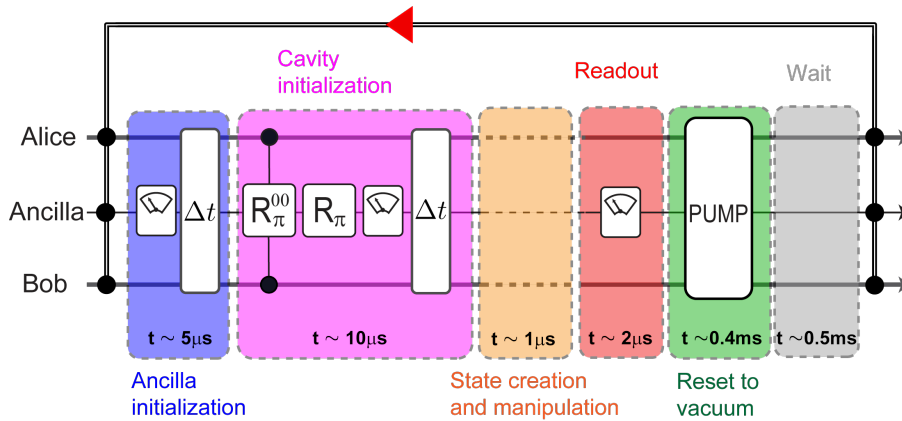

FIG. S3. **Data acquisition flow chart with state initialization and reset.** Purification of the initial ground state against equilibrium excitations is implemented by performing two additional readouts of the ancilla state preceding each run of the actual experiment. The first readout is performed without any ancilla/cavity manipulation, intended to filter out the cases where the ancilla starts in $|e\rangle$. Then two π-pulses of ancilla $|g\rangle$-$|e\rangle$ rotations are applied, with the first conditional on $|0\rangle_A|0\rangle_B$, and the second unconditional. The second readout of the ancilla state discriminates the presence or absence of photons in the two cavities, and allows filtering out the cases where either Alice or Bob starts with 1 or more photons. The pulse sequences for the cat state generation and tomography follow this initialization sequence, and we select data from runs where both readouts return the outcome of $|g\rangle$. We use a four-wave mixing method to reset the cavity state close to vacuum by applying three microwave pump tones at frequencies detuned from Alice, Bob and ancilla respectively for a duration of 400 μs.

onator mode using three parametric pumping tones. We apply this reset operation for 400 μs, and acquire our experimental data with a repetition cycle of about 900 μs.

Ideally, in thermal equilibrium at our base temperature (20 mK) all modes (Alice, Bob, or ancilla) of our quantum system should be in their ground state. However, in our experiment there is a non-negligible probability that any of the three modes is found in an excited state possibly due to insufficient thermalization. These erroneous excited state populations, about 8% for the ancilla and 2-3% for Alice and Bob, can reduce the fidelity of the subsequently-prepared quantum state and the parity measurement. To eliminate these effects, we perform two measurements as shown in Fig. S3 to "purify" the initial state of the system before we start each run of the experiment. This is implemented by post-selecting the cases where our experiment starts from the ground state, $|g\rangle|0\rangle_A|0\rangle_B$, before any non-trivial quantum operation is performed, which amounts to about 80% of the all the data acquired. It should be noted that the use of post-selection here is purely for experimental convenience and does not compromise the deterministic nature of the generation of cat states. One can in principle use real-time feedback to prepare the initial state and achieve a slightly higher data rate. No post-selection beyond the ground state initialization is applied in our analyses of the two-mode cat state.

D. Device Characterization

The Hamiltonian parameters and coherence properties of the device are mostly characterized by adapting established techniques, in particular, various forms of Ramsey interferometry. The measured coherence times of the Alice, Bob and the ancilla are listed in Table I of the main text, and a more complete list is provided in Table S2. We briefly comment on a few characterization methods that are noteworthy.

Measurement of the coherence of higher excited states of a superconducting transmon is a relatively new topic recently reported in Ref. 8. In addition to using a similar sequence to determine $T^*_{2,ef}$ between $|f\rangle$ and $|e\rangle$, we note that $T^*_{2,gf}$ (between $|f\rangle$ and $|g\rangle$) is more relevant to our experiment. This $T^*_{2,gf}$ time cannot be simply derived from $T^*_{2,ge}$ and $T^*_{2,ef}$, but can be determined by a Ramsey experiment starting from a $\frac{1}{\sqrt{2}}(|g\rangle + |f\rangle)$ superposition.

The coherence times of Alice and Bob are measured using

	T_1	T^*_2	T_{2E}	P_e
Ancilla $|e\rangle$	65-75 μs	30-45 μs	55-65 μs	7.5%
Ancilla $|f\rangle$	26-32 μs	12-24 μs[a]	20-30 μs[a]	0.5%
Alice	2.2-3.3 ms	0.8-1.1 ms	N/A	2-3%
Bob	1.2-1.7 ms	0.6-0.8 ms	N/A	2-3%
Readout	260-290 ns	N/A	N/A	<0.2%

[a] T^*_2=11-19 μs for $|f\rangle$ vs. $|g\rangle$, T_{2E}=18-26 μs for $|f\rangle$ vs. $|g\rangle$.

TABLE S2. Energy relaxation time (T_1), Ramsey coherence time (T^*_2) , coherence time with Hahn echo (T_{2E}), and thermal population of the excited state (P_e) of all components when applicable.

Ramsey interference of $|0\rangle$ and $|1\rangle$ Fock states following a Selective Number Arbitrary Phase (SNAP) gate[9] that prepares the Fock state superposition. This method, which is described in Ref. 1, extracts the T^*_2 without being affected by high-order nonlinearities (Fig. S4). Together with the measurement of the cavity T_1, we find the cavity pure dephasing time $T_\phi = 1/(\frac{1}{T^*_2} - \frac{1}{2T_1}) = 1.1 \pm 0.2$ ms for Alice and 0.9 ± 0.2 ms for Bob. Such pure dephasing times can be fully explained by their dispersive frequency shifts due to the thermal excitation of the transmon ancilla[1]. The rate of the $|g\rangle \rightarrow |e\rangle$ transition of the transmon, $\Gamma_\uparrow$, can be determined from its T_1 and thermal population of the $|e\rangle$ state, P_e: $\Gamma_\uparrow = P_e/T_1 = 7.5\%/(70~\mu s) = 1/(0.9$ ms). In addition, the cavity Ramsey experiment also allows extraction of the precise resonance frequency of the cavity. Over the course of 8 months while the device was continuously operated at 20 mK, we observed no slow drift of cavity frequency exceeding its linewidth (≈ 200 Hz).

The dispersive frequency shifts (χ's) are measured both in the frequency domain by spectroscopy techniques and in the time domain by a Ramsey-type qubit state revival experiment[10]) (Fig. S5). These techniques established previously for 2-level qubits, can both be extended for the 3-level artificial atom considered in this study. The latter measurement is also a valuable procedure for tuning up the joint parity measurement.

The self-Kerr effect of Alice or Bob (K_A or K_B terms in the Hamiltonian) can be characterized by the collapse and revival of a single-cavity coherent state[5]. In addition, with two long-lived cavities, we are able to directly measure the inter-cavity cross-Kerr effect (K_{AB}) by observing the frequency shift of Bob in response to the presence of photons in Alice.

E. Cat State Generation

The two-mode cat state is generated deterministically using conditional operations between the ancilla and the two cavities. As presented in the main text (Fig. 1C), the generation sequence is composed of the following steps[11]: 1) preparing ancilla superposition ($R^{ge}_{\pi/2}$), 2) displacements of Alice and Bob conditional on the ancilla state ($D^g_{2\alpha}$), realizing a three-way entangling gate, 3) conditional flip (reset) of ancilla (R^{00}_π), disentangling it from the cavity state, 4) unconditional displacements of Alice and Bob ($D_{-\alpha}$) to center the cat state in the phase space (which is a trivial step purely for convenience of presentation).

The conditional displacement ($D^g_{2\alpha}$) is the key step in this state generation process. Although this operation can be directly implemented using cavity drives with a bandwidth smaller than the dispersive interaction strength (χ^{ge}_i, i=A or B), such a method requires a rather long pulse duration (and therefore higher infidelity due to decoherence and Kerr effects). Alternatively, for each cavity we use two unconditional displacements separated by a wait time Δt in between to effectively realize $D^g_{2\alpha}$.

During the wait time Δt, due to the dispersive interaction, cavity coherent states in both cavities accumulate
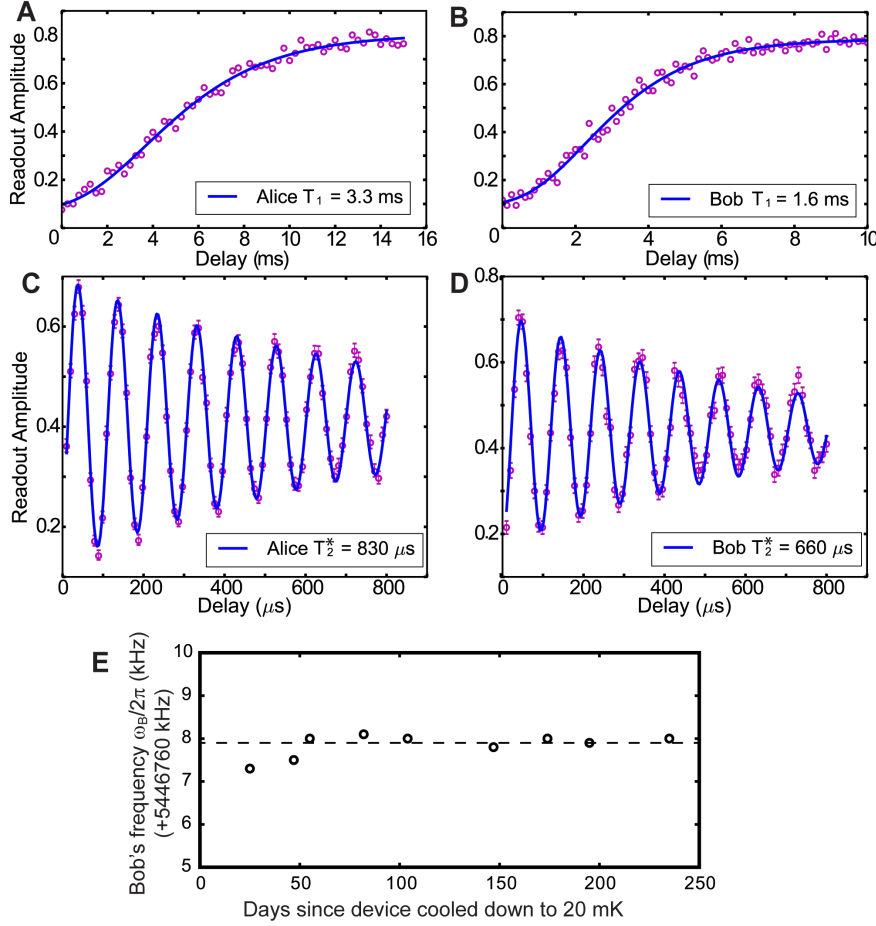
FIG. S4. **Measurement of cavity coherence. (A, B)** Measurement of the relaxation of a coherent state in Alice and Bob over time, which determine cavity relaxation times (T_1). The vertical axes represent the overlap of the (coherent) state with the vacuum state. **(C, D)** Ramsey interference experiment of a $\mathcal{N}(|0\rangle + |1\rangle)$ Fock state in Alice and Bob, which determine cavity coherence times (T_2^*). **(E)** Cavity resonance frequency of Bob extracted from Ramsey interference experiments over the course of eight months, showing long-term stability on the order of 100 Hz.

conditional phases of $\phi_i = \chi_i^{ge} \Delta t$ if the ancilla is in $|e\rangle$:

$$U(\Delta t) = \mathbb{I}_A \otimes \mathbb{I}_B \otimes |g\rangle\langle g| + e^{i\phi_A a^\dagger a} \otimes e^{i\phi_B b^\dagger b} \otimes |e\rangle\langle e| \quad (S2)$$

Using the IQ plane to describe the photon probability distribution in each cavity in the rotating frame, a coherent state $|\alpha'\rangle_i$ can be represented by a (Gaussian) circle that stays stationary when the ancilla is in $|g\rangle$, and rotates with the angular velocity χ_i^{ge} when the ancilla is in $|e\rangle$: $|\alpha'\rangle_i \rightarrow |\alpha' e^{i\chi_i^{ge}\Delta t}\rangle_i$. Therefore, this conditional phase gate can split the cavity coherent state in phase space when the ancilla is prepared in $\frac{1}{\sqrt{2}}(|g\rangle + |e\rangle)$, effectively realizing a conditional displacement. A similar strategy has been previously implemented for a single cavity[10]. The actual pulse sequences for creating the two-mode cat state and the resultant state evolution for the two cavity system are illustrated in Fig. S6.

In this work we have focused on studying the two-mode cat state $|\psi_\pm\rangle$. This state is equivalent to a cat state of the form $\mathcal{N}(|\sqrt{2}\alpha\rangle_C \pm |-\sqrt{2}\alpha\rangle_C)$ in a hybridized mode basis of $c^\dagger = \frac{1}{\sqrt{2}}(a^\dagger + b^\dagger)$. Cat-state control over the $c^\dagger$ mode alone would not be fundamentally more useful than controlling a single local mode (as in previous works) if we cannot access modes other than $c^\dagger$. However, it is easy to see that we can create cat states in Alice (or Bob) alone by omitting all pulses on Bob (or Alice) in Fig. S6. The resultant conventional single-mode cat state can be characterized by Wigner tomography of individual cavities (Fig. S7). Furthermore, we can reverse the cavity displacements in either Alice or

Bob in Fig. S6 to realize a cat state in the $\frac{1}{\sqrt{2}}(a^\dagger - b^\dagger)$ basis. The important message from the present experiment is that we can create cat states in an arbitrary basis spanned by two modes. In fact, it can be shown that the dispersive Hamiltonian permits universal quantum control of this system.[12][13]

F. Joint Parity Measurement

Measurement of the joint photon number parity, P_J, is critical to our study of two-cavity quantum states. Here we explain in detail the quantum operations and required system parameters to realize such measurements.

Photon parity measurement of a single-cavity quantum state using an ancilla qubit (using only $|g\rangle$ and $|e\rangle$ levels) has been previous demonstrated in Ref. 14 (see Fig. 1 therein). This single-cavity protocol is applicable to either one of our cavities when the other cavity is in the vacuum state. It uses the dispersive interaction χ_i^{ge} to map even-photon-number and odd-photon-number states in the cavity of interest (i=A or B) to different qubit levels. This is realized by two $\pi/2$ rotations of the qubit, $R_{\pi/2}^{ge}$ (around the same X-axis), separated by a wait time of π/χ_i^{ge}. For example, if Bob is in the vacuum state ($b^\dagger b = 0$), the conditional phase shift described in Eq. (S2) over the time $\Delta t = \pi/\chi_A^{ge}$ is:

$$U(\pi/\chi_A^{ge}) = C_\pi^A = \mathbb{I} \otimes |g\rangle\langle g| + e^{i\pi a^\dagger a} \otimes |e\rangle\langle e| \quad (S3)$$

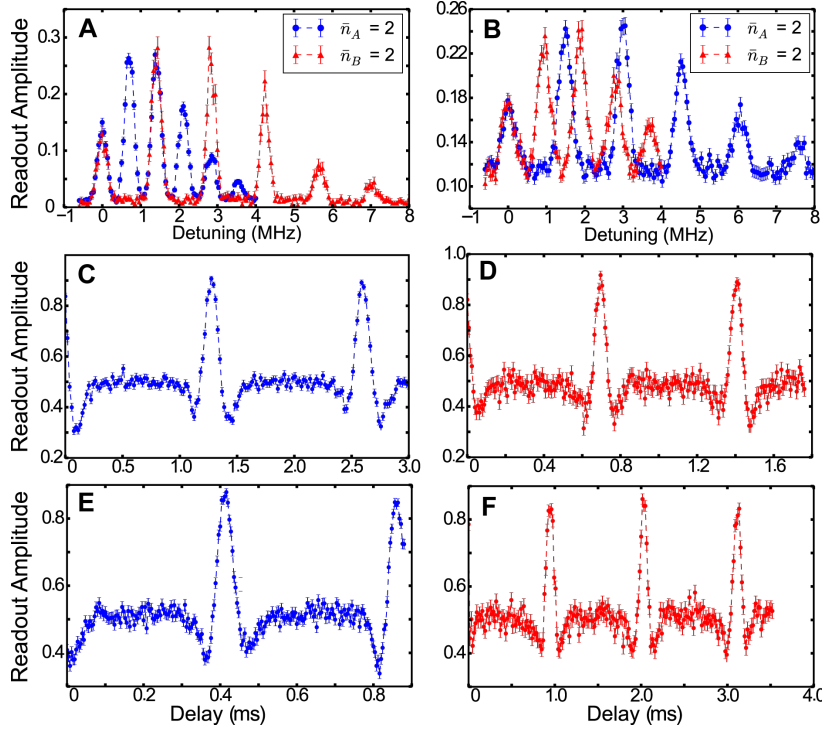FIG. S5. **Characterization of transmon-cavity dispersive coupling.** **(A)** Photon-number-splitting of the transmon $|g\rangle$-$|e\rangle$ transition frequency for a coherent state in Alice (blue) or Bob (red). The vertical axis represents the probability of exciting the $|g\rangle$-$|e\rangle$ transition with a microwave tone at a frequency marked by the horizontal axis. **(B)** Photon-number-splitting of the transmon $|e\rangle$-$|f\rangle$ transition frequency for a coherent state in Alice (blue) or Bob (red). **(C, D)** Revival of a transmon state $\mathcal{N}(|g\rangle + |e\rangle)$ in the presence of a coherent state in (C) Alice or (D) Bob. **(E, F)** Revival of a transmon state $\mathcal{N}(|e\rangle + |f\rangle)$ in the presence of a coherent state in (E) Alice or (F) Bob.
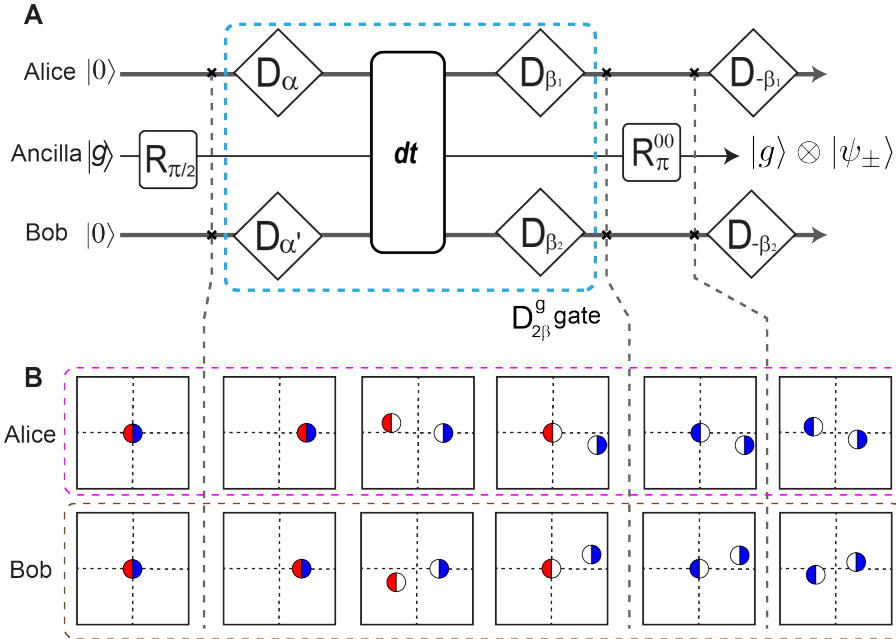

FIG. S6. **Experimental protocol for deterministic generation of the two-mode cat state.** (A) Microwave control pulse sequences for state generation, written in a general form that allows different amplitude in two cavities. (B) Cartoon representation of the step-by-step state evolution of Alice and Bob in their respective IQ planes. Blue and red indicate the cavity photon probability distributions associated with the ancilla in $|g\rangle$ and in $|e\rangle$ respectively. The parameters used for generating the two-mode cat state presented in the main text are $\alpha_1 = \alpha_2 = 2.25$, $\Delta t = 444$ ns, $\alpha_1' = 2.25 \times e^{-1.03i}$, $\alpha_2' = 2.25 \times e^{1.03i}$, $\alpha_1'' = 1.93 \times e^{-0.48i}$, $\alpha_2'' = 1.93 \times e^{0.65i}$. After arriving in the final state $|\psi_\pm\rangle$, we rotate the IQ reference frame so that $\alpha \approx 1.92$ is a real number.

This is equivalent to a qubit Z-rotation of π conditioned on the photon number in Alice being odd because $e^{i\pi a^\dagger a} = P_A$. Therefore the whole sequence $R^{ge}_{\pi/2} C^A_\pi R^{ge}_{\pi/2}$ flips the qubit if and only if the photon number parity in Alice is even, and subsequent readout of the qubit state measures the parity.

The control and measurement sequence described above can in principle be directly implemented in our experiment to measure the joint photon number parity if χ^{ge}_A is exactly equal to χ^{ge}_B. This is because for a wait time of $\Delta t = \pi/\chi^{ge}_A (= \pi/\chi^{ge}_B)$, from Eq. (S2) we have:

$$U(\pi/\chi^{ge}_i) = C^A_\pi C^B_\pi$$
$$= \mathbb{I} \otimes |g\rangle\langle g| + P_A P_B \otimes |e\rangle\langle e| \quad \text{(S4)}$$

Noting $P_J = P_A P_B$, an identical control sequence of $R^{ge}_{\pi/2} U(\Delta t) R^{ge}_{\pi/2}$ followed by a qubit readout would achieve the joint parity measurement. However, without strictly identical χ^{ge}_A and χ^{ge}_B, the phase accumulation in one cavity is faster than the other, and it is in general not possible to realize parity operators in both cavities simultaneously using this simple protocol. Moreover, for a general two-cavity quantum state, this sequence can not measure a single-cavity parity operator (P_A or P_B) due to inevitable entanglement between the ancilla and the photons in the other cavity during the process.

As noted in the main text, we introduce a technique for measuring P_J with less stringent requirements on Hamiltonian parameters by exploiting the $|f\rangle$-level of the ancilla.
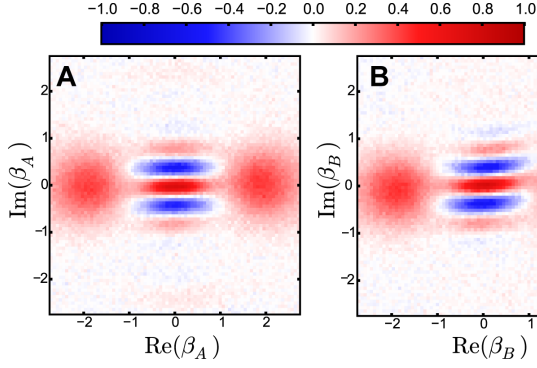
FIG. S7. **Wigner tomography of single-mode cat states.**
(A) Scaled single-cavity Wigner function of Alice, $\frac{\pi}{2}W_A(\beta_A)$, of the state $\mathcal{N}(|\alpha\rangle_A + |-\alpha\rangle_A) \otimes |0\rangle_B$. **(B)** Scaled single-cavity Wigner function of Bob of the state $|0\rangle_A \otimes \mathcal{N}(|\alpha\rangle_B + |-\alpha\rangle_B)$.

This method is most helpful when the $|e\rangle \rightarrow |g\rangle$ transition of the ancilla shows stronger interaction with Bob ($\chi_B^{ge} > \chi_A^{ge}$), while the $|f\rangle \rightarrow |e\rangle$ transition shows stronger interaction with Alice ($\chi_A^{ef} > \chi_B^{ef}$). This is physically realized by engineering the ancilla frequency to lie between the two cavities, i.e. $\omega_A < \omega_{ef} < \omega_{ge} < \omega_B$.

Considering the quantum state with two cavities and three ancilla levels in general, the unitary evolution for any wait time Δt is:

$$U(\Delta t) = \mathbb{I}_A \otimes \mathbb{I}_B \otimes |g\rangle\langle g| + e^{i\phi_A a^\dagger a} \otimes e^{i\phi_B b^\dagger b} \otimes |e\rangle\langle e|$$
$$+ e^{i\phi_A' a^\dagger a} \otimes e^{i\phi_B' b^\dagger b} \otimes |f\rangle\langle f| \quad (S5)$$

where

$$\phi_A = \chi_A^{ge}\Delta t, \qquad \phi_B = \chi_B^{ge}\Delta t$$
$$\phi_A' = \chi_A^{gf}\Delta t, \qquad \phi_B' = \chi_B^{gf}\Delta t \quad (S6)$$

Here we define $\chi_A^{gf} \equiv \chi_A^{ge} + \chi_A^{ef}$ and $\chi_B^{gf} \equiv \chi_B^{ge} + \chi_B^{ef}$. Therefore, the two cavities simultaneously acquire conditional phases in their coherent state components at relative rates that differ for $|e\rangle$ and $|f\rangle$.

One possible pulse sequence for such P_J measurement using three ancilla levels is shown in Fig. 1C of the main text and reproduced as Fig. S8A. For a given two-cavity quantum state Ψ_{AB}, We first use a $R_{\pi/2}^{ge}$ rotation to prepare the ancilla in $\frac{1}{\sqrt{2}}(|g\rangle + |e\rangle)$. Then a wait time Δt_1 imparts phases $\phi_{A1} = \chi_A^{ge}\Delta t_1$ and $\phi_{B1} = \chi_B^{ge}\Delta t_1$ to the two cavities for the $|e\rangle$ component of the state:

$$\Psi_{AB} \otimes \frac{1}{\sqrt{2}}(|g\rangle + |e\rangle)$$
$$\Rightarrow \frac{1}{\sqrt{2}}\left[\Psi_{AB} \otimes |g\rangle + e^{i\phi_{A1} a^\dagger a} e^{i\phi_{B1} b^\dagger b}\Psi_{AB} \otimes |e\rangle\right] \quad (S7)$$

Next, the $|e\rangle$ component in this intermediate state is converted to $|f\rangle$ by a π rotation in the $|e\rangle$-$|f\rangle$ space, R_π^{ef}. Subsequently a second wait time Δt_2 leads to a second simultaneous conditional phase gate, imparting phases $\phi_{A2} = \chi_A^{gf}\Delta t_2$ and $\phi_{B2} = \chi_B^{gf}\Delta t_2$ to the two cavities for the now

$|f\rangle$ component of the state:

$$\frac{1}{\sqrt{2}}\left[\Psi_{AB} \otimes |g\rangle + e^{i\phi_{A1} a^\dagger a} e^{i\phi_{B1} b^\dagger b}\Psi_{AB} \otimes |f\rangle\right] \Rightarrow$$
$$\frac{1}{\sqrt{2}}\left[\Psi_{AB} \otimes |g\rangle + e^{i(\phi_{A1}+\phi_{A2}) a^\dagger a} e^{i(\phi_{B1}+\phi_{B2}) b^\dagger b}\Psi_{AB} \otimes |f\rangle\right]$$
$$(S8)$$

The $|f\rangle$ component is then converted back to $|e\rangle$ by another R_π^{ef} pulse. If we can find Δt_1 and Δt_2 so that:

$$\phi_{A1} + \phi_{A2} = \chi_A^{ge}\Delta t_1 + \chi_A^{gf}\Delta t_2 = \pi$$
$$\phi_{B1} + \phi_{B2} = \chi_B^{ge}\Delta t_1 + \chi_B^{gf}\Delta t_2 = \pi \quad (S9)$$

the obtained quantum state is:

$$\frac{1}{\sqrt{2}}\left[\Psi_{AB} \otimes |g\rangle + P_J\Psi_{AB} \otimes |e\rangle\right] \quad (S10)$$

effectively realizing the simultaneous controlled π-phase gate ($C_\pi^A C_\pi^B$) in Eq. (S4). Finally a $R_{\pi/2}^{ge}$ pulse completes the projection of joint parity to the ancilla $|g\rangle$, $|e\rangle$ levels, ready for readout through the readout resonator.

The condition for finding non-negative solutions for Δt_1 and Δt_2 in Eq. (S9) is that $\chi_A^{ge} - \chi_B^{ge}$ and $\chi_A^{gf} - \chi_B^{gf}$ have opposite signs. In essence, the cavity that acquires phase slower than the other at $|e\rangle$ due to smaller χ_i^{ge} is allowed to catch up at $|f\rangle$ using its larger χ_i^{gf}.

It should be noted that such relative relation of the χ's is just a practically preferred condition rather than an absolute mathematical requirement. This is because parity mapping can be achieved whenever both cavities acquire a conditional phase of π modulo 2π. It is always possible to allow extra multiples of 2π phases applied to the cavity with stronger dispersive coupling to the ancilla, although it increases the total gate time and incurs more decoherence. The essential ingredient in engineering the P_J operator is the extra tuning parameter Δt_2 (in addition to Δt_1) that allows two equations such as Eq. (S9) to be simultaneously satisfied.

This extra degree of freedom also enables measurement of the photon number parity of a single cavity, P_A or P_B, for an arbitrary two-cavity quantum state. This can be realized with the same control sequences (Fig. S8A), choosing wait times such that one cavity acquires a conditional π phase (modulo 2π) while the other acquires 0 phase (modulo 2π). For example, to measure P_A we use Δt_1 and Δt_2 satisfying:

$$\phi_{A1} + \phi_{A2} = \chi_A^{ge}\Delta t_1 + \chi_A^{gf}\Delta t_2 = \pi \,(\text{mod}\,2\pi)$$
$$\phi_{B1} + \phi_{B2} = \chi_B^{ge}\Delta t_1 + \chi_B^{gf}\Delta t_2 = 0 \,(\text{mod}\,2\pi) \quad (S11)$$

Fig. S8B shows an alternative version of joint parity mapping protocol, which uses more ancilla operations, but is better adapted to to a larger parameter space of χ's. In this protocol, the ancilla spends time at the $|e\rangle$-$|f\rangle$ superposition so that conditional phases proportional to χ_i^{ef} are applied to the cavities. To achieve joint parity mapping, the two time intervals Δt_1 and Δt_2 should satisfy:

$$\phi_{A1} + \phi_{A2} = \chi_A^{ef}\Delta t_1 + \chi_A^{gf}\Delta t_2 = \pi \,(\text{mod}\,2\pi)$$
$$\phi_{B1} + \phi_{B2} = \chi_B^{ef}\Delta t_1 + \chi_B^{gf}\Delta t_2 = \pi \,(\text{mod}\,2\pi) \quad (S12)$$
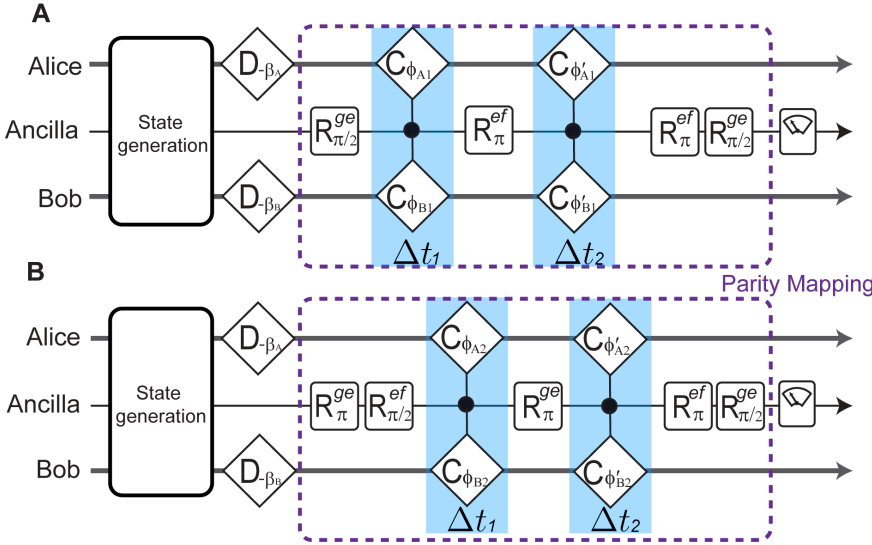
FIG. S8. **Two experimental protocols for joint parity measurement.** (A) The same control pulse sequences shown in Fig. 1(C) of the main text. The conditional phase gates are realized by the wait time Δt_1 and Δt_2 while the ancilla is in a superposition state. Here $\phi_A = \chi_A^{ge}\Delta t$, $\phi_B = \chi_B^{gf}\Delta t$, $\phi'_A = \chi_A^{gf}\Delta t$, $\phi'_B = \chi_B^{gf}\Delta t$. We use $\Delta t_1 = 0$ ns, and $\Delta t_2 = 184$ ns for P_J measurements presented in the main text, which involves a small systematic phase error in the parity mapping operation. One can choose larger Δt_1 and Δt_2 to avoid this error but at the cost of more decoherence and Kerr effects. (B) An alternative parity measurement sequence involving the $|e\rangle$-$|f\rangle$ superposition of the ancilla, where $\phi_A = \chi_A^{ef}\Delta t$, $\phi_B = \chi_B^{ef}\Delta t$ instead. We use $\Delta t_1 = 28$ ns, and $\Delta t_2 = 168$ ns for P_J measurements presented in Fig. S10. This method reduces the parity mapping phase error at the cost of more ancilla pulse errors.

which can avoid the use of extra 2π phases to $\chi_A^{ef} - \chi_B^{ef}$ has opposite sign versus $\chi_A^{gf} - \chi_B^{gf}$.

Experimentally, choices of the parity mapping sequence and gate times involve trade-offs in various aspects such as pulse speed/bandwidth and coherence time. We have measured joint parity (and subsequently Wigner functions) using both protocols. For the sequence of Fig. S8A, $\Delta t_1 = 0$, $\Delta t_2 = 184$ ns was experimentally implemented. For the sequence of Fig. S8B, $\Delta t_1 = 28$ ns, $\Delta t_2 = 168$ ns was used. The actual effective wait time was longer due to the non-zero duration (16 ns) of each ancilla rotation. The first protocol, with this choice of wait times, does not yield the exact π phases required for exact parity mapping (We estimate $\phi_{A1} + \phi_{A2} = 0.97\pi$ and $\phi_{B1} + \phi_{B2} = 1.03\pi$. These phase errors lead to an estimated infidelity of the joint parity measurement of about 3% for the two-cavity states in this study (Fig. S9). Exact phases can be achieved with longer wait times so that $\phi_{A1} + \phi_{A2} = 3\pi$ and $\phi_{B1} + \phi_{B2} = 5\pi$, but the infidelity due to decoherence and high-order Hamiltonian terms outweighs the benefits. In principle, the second protocol that achieves exact π phases at relatively short total gate time should be more advantageous. However, using the second protocol, we observe visibly identical results of joint Wigner tomography of the two-mode cat states with fidelity nearly equal to the first protocol (Fig. S10). This is attributed to the extra infidelity from the more complicated ancilla rotations involved in the second protocol (due to pulse bandwidth limitations and unwanted ancilla population mixing, see Section L of this Supplementary). All joint Wigner tomography shown in the main text are measured using the first protocol (matching Fig. 1C).

Single cavity Wigner tomography is also performed using the protocol of Fig. S8A, with $\Delta t_1 = 688$ ns, $\Delta t_2 = 0$ for P_A, and $\Delta t_1 = 660$ ns, $\Delta t_2 = 204$ ns for P_B. Moreover, for P_A measurement the R_π^{ef} pulses were skipped, taking advantage of the fact that $\chi_B^{ge} \approx 2\chi_A^{ge}$.

SUPPLEMENTARY TEXT

G. Extended Data for Two-mode Cat State

The joint tomography of a two-cavity quantum state is described by a four dimensional joint Wigner function $W_J(\beta_A, \beta_B)$. The most informative plane cuts of W_J, along $\text{Re}(\beta_A)$-$\text{Re}(\beta_B)$ and $\text{Im}(\beta_A)$-$\text{Im}(\beta_B)$, have been presented in the main text. This section provides additional data of our measurement on the joint quantum state of Alice and Bob.

Fig. S11 shows the joint Wigner function of $|\psi_+\rangle$ ($\alpha = 1.92$) measured in the natural single-cavity IQ planes, or plane cuts of W_J along $\text{Re}(\beta_A)$-$\text{Im}(\beta_A)$ and $\text{Re}(\beta_B)$-$\text{Im}(\beta_B)$ respectively (and through the origin). Both plane cuts contain interference fringes along the imaginary axis as expected. No features of Gaussian coherent states are observed in either figure because the underlying coherent states $|\alpha\rangle_A|\alpha\rangle_B$ and $|-\alpha\rangle_A|-\alpha\rangle_B$ are located outside these plane cuts.

To assist visualization of the two-mode cat state, the joint Wigner function of $|\psi_-\rangle$ ($\alpha = 1.92$) is further presented as a movie, which is a direct extension of Fig. 3 of the main text. It shows 21 frames of $\text{Re}(\beta_A)$-$\text{Re}(\beta_B)$ plane cuts as a function of the $\text{Im}(\beta_A)$,$\text{Im}(\beta_B)$ coordinates.

Via measurement of the joint photon number parity, we have inferred that the state $|\psi_+\rangle$ (or $|\psi_-\rangle$) has an even (or odd) number of photons in the two cavities combined. Taking advantage of the fact that $\chi_A^{gf} \approx \chi_B^{gf}$ in our device, this joint parity property can be directly illustrated by measuring the statistical distribution of the total photon number in the two-mode cat state. The measurement is realized by spectroscopic probe of the $|g\rangle \to |f\rangle$ two-photon transition (which is a second-order process occurring at much higher driving power than $|g\rangle \to |e\rangle$ or $|e\rangle \to |f\rangle$ transitions). As shown in Fig. S12 for the odd parity state $|\psi_-\rangle$ (α=1.92), the $(|g\rangle \to |f\rangle)/2$ spectral line of the ancilla is split into multiple peaks corresponding to different cavity
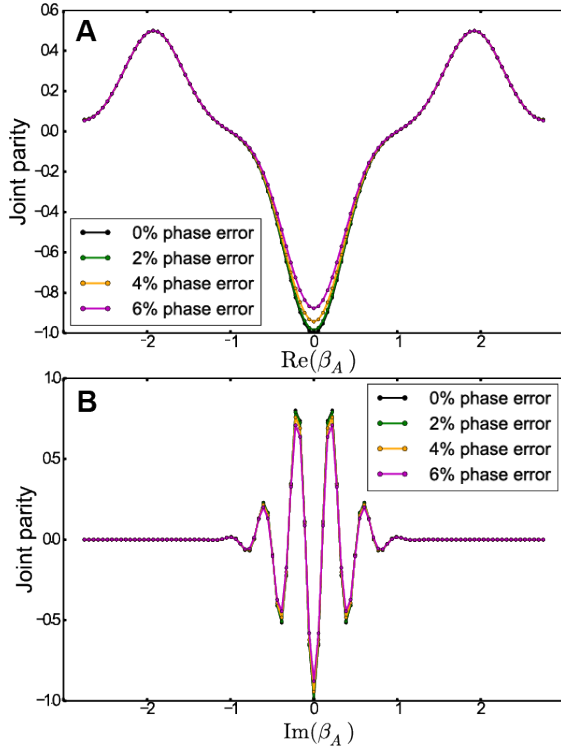
FIG. S9. **Sensitivity of Wigner tomography to the phase error of joint parity mapping.** By numerical simulation, we consider non-ideal joint parity mapping where an operator $\mathbb{I} \otimes |g\rangle\langle g| + e^{-i\epsilon\pi a^\dagger a} \otimes e^{i\epsilon\pi b^\dagger b} P_J \otimes |e\rangle\langle e|$ is applied. ($\epsilon = 0$ corresponds to perfect joint parity mapping.) **(A)** The $\mathrm{Re}(\beta_A)=\mathrm{Re}(\beta_B)$ and **(B)** the $\mathrm{Im}(\beta_A)=\mathrm{Re}(\beta_B)$ line-cuts of the simulated scaled "joint Wigner function" $\langle e^{i\epsilon\pi(b^\dagger b - a^\dagger a)} P_J \rangle$ are plotted for the two-mode cat state $|\psi_-\rangle$ ($\alpha = 1.92$) for various ϵ. No other non-ideality is included in this simulation. Our measurement condition using the protocol in Fig. S8A corresponds to $\epsilon \approx 0.03$.

H. Two-mode Cat State of Larger Size

The methods to generate and measure cat states shared in two cavities can in principle be applicable to arbitrary photon numbers. We briefly measured the core features in the joint Wigner functions of 2-mode cat states with larger and generally different numbers of photons in Alice and Bob, i. e. $\mathcal{N}\big(|\alpha_1\rangle_A|\alpha_2\rangle_B - |-\alpha_1\rangle_A|-\alpha_2\rangle_B\big)$. Fig. S13 shows the $\mathrm{Im}(\beta_A)$-$\mathrm{Im}(\beta_B)$ plane-cuts of $\langle P(\beta_A, \beta_B)\rangle$ for two such states. The number or the density of interference fringes increases with the total photon number, proportional to $\sqrt{\alpha_1^2 + \alpha_2^2}$. The largest state we have measured has a cat size of $S = (2\alpha_1)^2 + (2\alpha_2)^2 = 80$ photons, limited mostly by room temperature electronics. The contrast of the measured Wigner function decreases with increasing cat size, indicating lower fidelity in the prepared two-mode cat state and the joint parity measurement. The decreased fidelity is due to a combination of stronger decoherence and ancilla rotation infidelity due to bandwidth constraints.
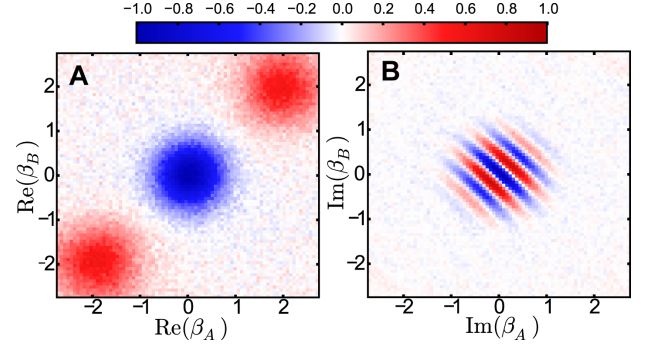

FIG. S10. **Joint Wigner function remeasured using an alternative parity mapping protocol.** To perform the same joint Wigner tomography of the same state ($|\psi_-\rangle$ with $\alpha = 1.92$) as shown in Fig. 3 of the main text, we can also use an alternative joint parity mapping protocol (shown in Fig. S8B). The resultant 2D plane cuts of the scaled Wigner function, $\langle P_J(\beta_A, \beta_B)\rangle$ are almost identical to Fig. 3, where the measured minimum joint parity is about -0.80.
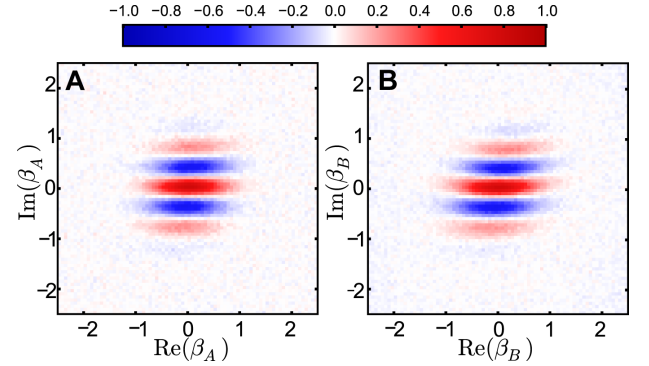

FIG. S11. **Joint Wigner function of the two-mode cat state along the single-cavity I-Q plane.** 2D plane cuts of the scaled joint Wigner function, $\langle P_J(\beta_A, \beta_B)\rangle$, of the state $|\psi_+\rangle$ ($\alpha = 1.92$) along **(A)** the axes $\mathrm{Re}(\beta_A)$-$\mathrm{Im}(\beta_A)$ and **(B)** the axes $\mathrm{Re}(\beta_B)$-$\mathrm{Im}(\beta_B)$.

I. Extended Data for Product Cat State

In an illustrative comparison with the two-mode cat state, in Fig. 4B of the main text we have shown joint tomography of an approximate product state of two independent cat states, $\mathcal{N}'(|\alpha\rangle_A - |-\alpha\rangle_A) \otimes (|\alpha\rangle_B - |-\alpha\rangle_B)$. We generate this "product cat state" using post-selection after QND parity measurement: A single-mode cat state in Bob is first created while Alice is in vacuum state (using the protocol described near the end of Section refsec:qcmap). Then a coherent state is prepared in Alice, followed by a single-cavity parity measurement of Alice, P_A. This measurement projects Alice to even or odd cat state $(\mathcal{N}(|\alpha\rangle_A \pm |-\alpha\rangle_A))$[14] while the cat state in Bob stays intact. We post-select odd parity from the outcome of P_A measurement, obtaining the product cat state for subsequent tomography. One can confirm the presence of independent single-mode cat states by performing Wigner tomography of individual cavities, $W_A(\beta_A)$ and $W_B(\beta_B)$ (Fig. S14). Indeed, the Wigner function of each cavity is similar to a cat state (i.e. Fig. S7) containing two coherent state components with interference fringes in between. This is in striking contrast to $W_A(\beta_A)$ and $W_B(\beta_B)$ of a two-mode (entangled) cat state (Fig. 2
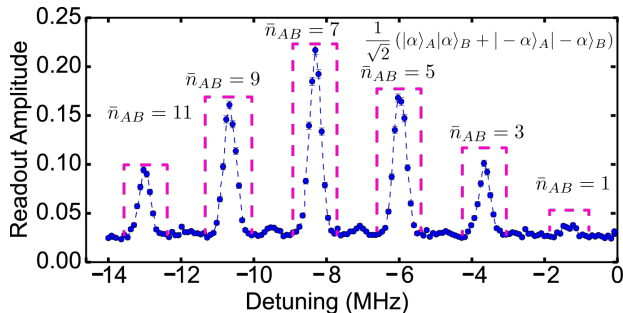
photon numbers, but only peaks associated with odd total number of photons are present.

FIG. S12. **Spectroscopic measurement of the two-mode cat state.** The data points show the probability of exciting the $|g\rangle \to |f\rangle$ two-photon transition of the transmon ancilla as a function of the drive frequency ω_d after an odd-parity two-mode cat state $|\psi_-\rangle$ ($\alpha = 1.92$) is prepared in Alice and Bob. Such two-photon transitions can be excited at $\omega_{gf/2} = (\omega_{ge} + \omega_{ef})/2 = 4.82047$ GHz if both cavities are in the vacuum state, but shifts towards lower frequency by $\chi_A^{gf}/2$ for each photon in Alice and or $\chi_B^{gf}/2$ for each photon in Bob. Because $\chi_A^{gf} \approx \chi_B^{gf}$, each peak in the spectrum can be identified with a total photon number in two cavities. This measurement therefore shows the probability distribution of total photon numbers. Only peaks associated with odd total number of photons are pronounced in the measurement, confirming the odd joint parity of the state $|\psi_-\rangle$.
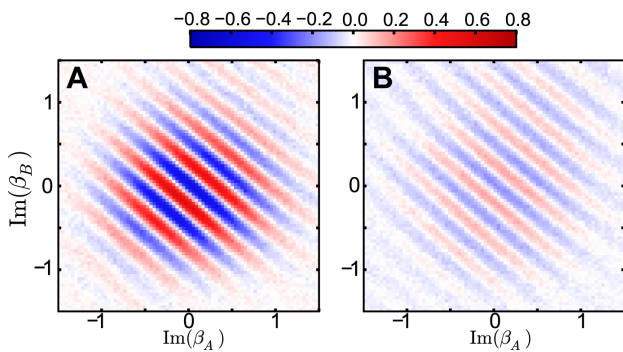

FIG. S13. **Interference fringes of two-mode cat states of larger size.** 2D plane-cuts of the scaled Wigner function $\langle P_J(\beta_A, \beta_B)\rangle$ along $\text{Im}(\beta_A) - \text{Im}(\beta_B)$ axes for two-mode cat states $|\psi_-\rangle$ with **(A)** $\alpha = 2.7$ in Alice and 3.1 in Bob, and **(B)** $\alpha = 3.0$ in Alice and 3.3 in Bob.
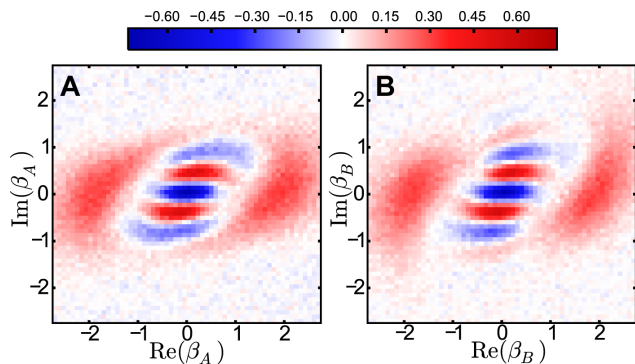

FIG. S14. **Single-cavity Wigner tomography of the product cat state.** The scaled single-cavity Wigner function, $W_A(\beta_A)$ and $W_B(\beta_B)$, of the same quantum state presented in Fig. 4B of the main text. This state is intended to be a product state of a cat state in Alice and a cat state in Bob, or $\mathcal{N}'(|\alpha\rangle_A - |-\alpha\rangle_A) \otimes (|\alpha\rangle_B - |-\alpha\rangle_B)$.

of the main text), where each cavity, when analyzed on its own, only contains a statistical mixture of two coherent states.

Fig. S14 also shows that the coherent state components in the product cat state are significantly distorted. This is due to the Kerr effects from the higher-order Hamiltonian terms that accumulates between the measurement-based state generation and the next measurement for tomography. Our device parameters are not optimal for such repetitive measurements due to the relatively slow readout speed (unable to repeat faster than $\sim 3\,\mu s$, or about $10\times$ the lifetime of the readout resonator). It should be noted that it is possible to create product cat state deterministically (without reliance on readout) while compensating for Kerr effects using numerically optimized control pulses[15]. In addition, future experiments can add separate ancillae coupled to Alice and Bob to further facilitate independent quantum operations of individual cavities.

J. State Reconstruction

Although features of the measured joint Wigner function can be compared intuitively with the ideal two-mode cat state, a full density matrix reconstruction is required to rigorously evaluate the fidelity of the quantum state. We perform this state reconstruction using maximum likelihood estimation for an over-complete data set of $W_J(\beta_k^{(A)}, \beta_k^{(B)})$ ($k \in \{1, \ldots, N_{\text{disp}}\}$) at N_{disp} different sampling points of the 4D phase space.

For each point of the joint Wigner function, we prepare N_{rep} copies of our state, perform the displacements $D_k \equiv D_A(\beta_k^{(A)})D_B(\beta_k^{(B)})$, and measure the joint parity $P_J = P_A P_B$, so that:

$$W_J(\rho, \beta_k^{(A)}, \beta_k^{(B)}) = \frac{4}{\pi^2}\, \text{Tr}[\rho D_k P_J D_k^\dagger] \tag{S13}$$

It is convenient to represent the measurement we perform as a POVM element $\Pi = (P_J + 1)/2$ which has eigenvalue 1 when $P_J = 1$ and eigenvalue 0 when $P_J = -1$, and consequently whose expectation value can be interpreted as the probability to observe even joint parity.

Note that these measurement outcomes can be written in two equivalent ways:

$$\text{Tr}[\rho(D_k \Pi D_k^\dagger)] \equiv \text{Tr}[\rho \Pi_k], \tag{S14}$$

and

$$\text{Tr}[(D_k^\dagger \rho D_k)\Pi] \equiv \text{Tr}[\rho_k \Pi]. \tag{S15}$$

This is to say that our experiment can be considered as a set of measurements Π_k used to characterize a state ρ, or as a set of states ρ_k used to characterize a measurement Π. Ideally, one would like to characterize both Π and ρ simultaneously, since the expected infidelity in these two operations are comparable. However, doing so would require a set of trusted operations beyond just displacements, as well as a squaring in number of measurements required. In light of this, we have performed state tomography assuming that our measurement operator is as designed, and acknowledging that the infidelity reported is a combination of the state preparation infidelity and measurement operator infidelity.

Let n_k be the number of times we observe $P_J = 1$ at the k-th sampling point (out of a total of N_{rep} repetitions). Our state reconstruction looks for the density matrix $\hat{\rho}_{ML}$ that maximizes the likelihood function:

$$\hat{\rho}_{\text{ML}} = \underset{\rho}{\text{argmax}}\, \mathcal{L}(\rho) \qquad (S16)$$

Here the likelihood $\mathcal{L}(\rho)$ is the probability of seeing the data n_k assuming ρ. For a fixed k, n_k should follow a binomial distribution:

$$\mathcal{L}(\rho) = \prod_k P(n_k|\rho)$$
$$= \prod_k \binom{N_{\text{rep}}}{n_k} (p_k(\rho))^{n_k} (1 - p_k(\rho))^{N_{\text{rep}}-n_k} \qquad (S17)$$

p_k is computed from the joint Wigner of ρ:

$$p_k(\rho) = \text{Tr}[\rho_k \Pi]$$
$$= \frac{1}{2}(\text{Tr}[\rho_k P_A P_B] + 1)$$
$$= \frac{1}{2}\left(\frac{\pi^2}{4} W_J(\rho, \beta_{k_A}, \beta_{k_B}) + 1\right) \qquad (S18)$$

What remains is to find an efficient method of calculating $W_J(\rho, \beta_A, \beta_B)$. To do so, write down ρ in the tensor Fock state basis, truncated to some maximum photon number N_{cutoff}:

$$\rho = \sum_{i,j,k,l=1}^{N_{\text{cutoff}}} \rho_{ijkl} |ij\rangle\langle kl| \qquad (S19)$$

Next use the linearity of W_J in ρ to identify the contribution from each component ρ_{ijkl}:

$$W_J(\rho, \beta_k^{(A)}, \beta_k^{(B)}) = \frac{4}{\pi^2}\, \text{Tr}[\rho D_k P_A P_B D_k^\dagger]$$
$$= \frac{4}{\pi^2} \sum_{ijmn} \rho_{ijmn}\langle mn|D_k P_A P_B D_k^\dagger|ij\rangle$$
$$= \frac{4}{\pi^2} \sum_{ijmn} \rho_{ijmn} K_{mi}(\beta_k^{(A)}) K_{nj}(\beta_k^{(B)}), \qquad (S20)$$

We can compute the matrix elements $K_{mn}(\beta) \equiv \langle m|D(\beta)PD(\beta)^\dagger|n\rangle$ in the same way one would in standard Wigner state tomography[16], i.e.

$$K_{mn}(\beta) \equiv \langle m|D(\beta)PD(\beta)^\dagger|n\rangle$$
$$= e^{-|\beta|^2}(-1)^m (2\beta)^{(n-m)} \sqrt{\frac{m!}{n!}} L_m^{(n-m)}(|\beta|) \quad (S21)$$

where $L_m^{(n-m)}$ is a generalized Laguerre polynomial.

In order to be a physical solution, ρ must be positive semidefinite with $\text{Tr}[\rho] = 1$. To account for this, we adjust the optimization problem

$$\hat{\rho}_{\text{ML}} = \hat{A}\hat{A}^\dagger$$
$$\hat{A} = \underset{A}{\text{argmax}}\, f(A)$$
$$f(A) = \ln \mathcal{L}(AA^\dagger) - \lambda(\text{Tr}[AA^\dagger] - 1)^2 \qquad (S22)$$

where now A can be any complex matrix, and λ is a Lagrange multiplier whose value must be greater than some threshold in order for the trace constraint to be satisfied. In practice, the value of λ can simply be increased until the deviation of the trace from unity is sufficiently small.

To solve the optimization problem for the two-mode cat state, $|\psi_+\rangle$, we first specify the photon number truncation N_{cutoff}. Based on the expected state with $\alpha \approx 1.92$, $\bar{n} = |\alpha|^2 \approx 3.69$, according to Poissonian statistics we must use $N_{\text{cutoff}} > 10$ to make the probability of having more than N_{cutoff} photons less than 0.1%. In practice, we take $N_{\text{cutoff}} = 12$, resulting in a system dimension $d = N_{\text{cutoff}}^2 = 144$, and $d^2 = 20736$ real parameters in the density matrix. (Note we have measured at $N_{\text{disp}} = 155,600$ different sampling points to form an overcomplete data set for the reconstruction.) Because the number of parameters is so large, it is necessary to compute the gradient $\frac{\partial f}{\partial A_{ij}}$ of the cost function with respect to the parameters, and to use a gradient-aware optimization routine, such as the BFGS algorithm.

After performing the reconstruction, we can extract several metrics about the state. The largest pure state overlap is given by the largest eigenvalue $\lambda_{\max}(\rho) \approx 0.824$. The purity is $\text{Tr}[\rho^2] \approx 0.68$. The state of form $|\psi\rangle = |\alpha, \alpha\rangle + |-\alpha, -\alpha\rangle$ with highest fidelity is $\alpha = 1.903$, with $\langle\psi|\rho|\psi\rangle \approx 0.803$. The state of form $|\psi\rangle = |\alpha_A, \alpha_B\rangle + e^{i\phi}|-\alpha_A, -\alpha_B\rangle$ with highest fidelity is $\alpha_A = 1.881$, $\alpha_B = 1.922$, $\phi = -0.1$ with $\langle\psi|\rho|\psi\rangle \approx 0.805$. Given the measured joint parity of 0.81 for the two-mode cat state, the highest possible fidelity one could expect is approximately 0.9, which would arise from a 90%-10% mixture of the ideal target state and a state of opposite parity (such as produced by a single-photon loss). Our reconstruction finds the parity of the dominant eigenvector to be 0.97, and the parity of the next few eigenvectors to be small and positive. This indicates that single-photon loss is not the dominant error mechanism affectubg the state generation, as will be discussed in Section L.

K. Parity Decay

We have briefly studied the decoherence of the two-mode cat state by measuring the decay of the joint photon number parity over time (Fig. S15). This is a convenient method without performing full tomography to gain insight into the major decoherence mechanism that occurs after the two-mode cat state has been created: photon loss in either of the two cavities. The observed decay of the joint parity is consistent with the combined photon loss in the two high-Q superconducting cavities:

$$P_J(t) = P_J(0) \exp\left[-2\alpha^2(2 - e^{-t/\tau_A} - e^{-t/\tau_B})\right] \quad (S23)$$

The parity decay takes the form of an "exponential with exponential" because the rate of parity decay is proportional to the photon numbers and therefore decreases over time. This equation is only applicable when the total photon number is far from zero. (The parity eventually approaches +1 as the cavities decay to the vacuum state.)

Since the parity initially decays at twice the total photon loss rate, it is still informative to consider a characteristic
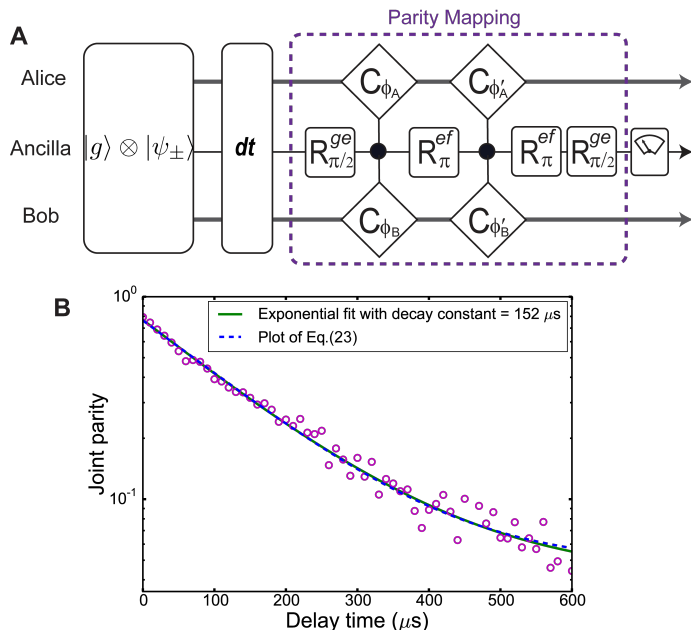
FIG. S15. **Joint parity decay. (A)** Measurement sequence used to monitor the decay of joint parity. After preparing the two-mode cat state, a variable delay is implemented before reading out the joint parity at the origin. **(B)** The measured joint parity at the origin as a function of the variable delay time. Green curve is a fit to a simple exponential decay, which gives a decay constant of 152 μs. Blue dashed line shows the plot according to the functional form described in Eq. (S23) using $\alpha = 1.92$, $\tau_A = 2.6$ ms, and $\tau_B = 1.5$ ms.

time of parity decay during a time span much shorter than the cavity lifetimes so that the cavity photon numbers are approximately constant. We observe a decay time of about 150 μs for the state $|\psi_+\rangle$ with $\alpha = 1.92$ based on a single exponential fit of the parity decay. This can be well explained by taking the (average) measured cavity lifetimes $\tau_A = 2.6$ ms, $\tau_B = 1.5$ ms and considering the average photon number over a span of 600 μs after the initial state generation $\bar{N}_A \approx 3.3$, $\bar{N}_B \approx 3.0$, so that $2(\frac{\bar{N}_A}{\tau_A} + \frac{\bar{N}_B}{\tau_B}) \approx 1/(150\ \mu s)$.

The parity decay measurement is not sensitive to other decoherence processes such as cavity frequency shifts due to transmon thermal jumps ($|g\rangle \to |e\rangle$ and subsequent $|e\rangle \to |g\rangle$ jumps). However, this effect is expected to induce a cavity dephasing with a relatively long time constant of about 900 μs, and should be further improved with better thermalization of the device.

It is worth noting that the coherence time of this complex two-mode cat state (at $\alpha = 1.92$ with a cat size of 30 photons) is longer than the most coherent superconducting qubit reported so far[17], owing to the superior coherence property of the 3D cavities. This illustrates an important advantage in using the cavity states as quantum memories in cQED[112] or as logical qubits[18] in addition to the potential simplification of error correction operations.

L. Error Sources

The fidelity of the generation and measurement of cat states is limited by various factors as listed in Table S3.

Because the joint parity of the two-mode cat state is the simplest figure of merit for evaluating the overall fidelity, we further focus on analyzing the errors contributing to the loss of contrast in the measured $P_J = \pm 0.81$ for $|\psi_\pm\rangle$ with $\alpha = 1.92$ (compared with the ideal value of $P_J = \pm 1$). The measuredvalue corresponds to a single point in the scaled joint Wigner function at the origin, $(\pi^2/4)W_J(\beta_A = 0, \beta_B = 0)$, but is the most representative point. We note again that there are mechanisms affecting the fidelity of the entire quantum state without directly contributing to the measured parity of the cat state, most notably the Kerr effects. However, via density matrix reconstruction we found that the fidelity of the full state is also close to 81%, indicating that the most significant errors can be understood by analyzing P_J of the state alone.

Many contributions to the loss of parity contrast can be estimated from system parameters and tested by controlled experiments. Contributions from ancilla and cavity decoherence are estimated to be about 5% in total from their respective coherence times and the gate times. Contrast loss in measured parity due to infidelity of the single-shot readout is twice the readout error rate and determined to be about 2.5%. We estimate about 2% loss of parity contrast due to state initialization errosr (experiments starting not from $|g\rangle|0\rangle_A|0\rangle_B$), which is primarily due to $|g\rangle \to |e\rangle$ thermal transition of the ancilla during the relatively slow initial state purification protocol. These estimates are consistent with measurements of ancilla Rabi oscillations between ($|g\rangle$ and $|e\rangle$) (96-97% of full contrast) and the parity of single-cavity cat states in either Alice or Bob ($\sim$90% of full contrast).

Additional infidelity arises in measurement of the two-mode cat state in our experiment, which can be primarily attributed to imperfections associated with mapping the joint photon number parity to the ancilla state. One source of error as discussed in Section **??** is the non-ideal waiting time Δt_1 and Δt_2 used in the controlled-phase gate, where Alice and Bob acquire phases different from π by $\pm 3\%$, causing a joint parity measurement infidelity of about 3%.

Another major source of error is from the bandwidth constraint on the ancilla pulses. Ideally, the ancilla operations described in our joint parity mapping (Fig. S8) require both infinite bandwidth (in order to be completely independent of cavity photon numbers) and no spectral overlap with unwanted ancilla transitions (in order to minimize state leakage out of the intended ancilla levels), which are conflicting requirements. We have used Gaussian pulses with $\sigma_\omega = 2\pi \cdot 40$ MHz and duration of 16 ns for ancilla rotations as a compromise. The influence of multiple levels of a transmon under fast microwave drive has been studied before, but mostly limited to $|g\rangle$-$|e\rangle$ operations, where state leakage to $|f\rangle$ is a second-order effect on the computation (proportional to leakage population, or amplitude squared). In our control pulses, we have implemented derivative removal via adiabatic gate (DRAG)[19] developed for two-level qubits to correct for the presence of the third level. However, it is known that the standard DRAG technique does not fully address state leakage[20], which has a first-order effect to our joint parity mapping utilizing three computational levels. Furthermore, high-fidelity rotations in the $|e\rangle$-$|f\rangle$ space require correction for the presence of both $|g\rangle$ and $|h\rangle$ (the

	Assessment	Estimated infidelity
ancilla initialization	$\sim 0.5\%$ probability not in $|g\rangle$	$\sim 1\%$
cavity initialization	$\sim 0.5\%$ probability not in $|0\rangle_A|0\rangle_B$	$\sim 1\%$
readout infidelity	1.0-1.5% error rate	2.5%
ancilla decoherence in state generation	$|g\rangle$-$|e\rangle$ superposition for 0.65 μs	2.2%
pulse error in state generation	imperfect spectral selectivity of R_π^{00}	$\sim 1\%$
ancilla decoherence in parity mapping	$|g\rangle$-$|e\rangle$ & $|g\rangle$-$|f\rangle$ superposition for 0.25 μs	2.2%
timing (phase) error in parity mapping	$\pm 3\%$ phase error in C_π^A and C_π^B	$\sim 3\%$
pulse error in parity mapping	population mixing in $|g\rangle$-$|e\rangle$-$|f\rangle$ rotations	$\sim 5\%$
photon loss in two cavities	3.7-7.3 photons in each cavity for 0.9 μs	0.9%
Total		$\sim 19\%$

TABLE S3. Estimated contribution to the loss of contrast in the measured joint parity of the two-mode cat state, $|\psi_\pm\rangle$ ($\alpha = 1.92$), from various error sources.

fourth transmon level) not yet considered in the literature. Last but not least, optimal ancilla rotations in the presence of cavity photons also remain to be developed. We attribute the unaccounted loss of contrast in P_J (about 5%) to such control pulse errors in parity mapping. This is consistent with a controlled test that measures Ramsey interference of the ancilla $|g\rangle$-$|f\rangle$ superposition in the presence of cavity coherent states. This experiment uses very similar pulse sequences to joint parity mapping but does not incur errors associated with cat state generation, parity mapping phase and cavity initialization errors, and shows a contrast of 89%.

Based on these semi-quantitative analyses of error contributions listed in Table S3, one can further categorize the total 19% loss of contrast in the joint parity to be about 6% due to imperfection of the state preparation and 13% from the infidelity (or loss of visibility) of the joint parity measurement. Because there is no simple way to independently determine the visibility of the parity measurement (which is photon-number-dependent due to pulse errors), we do not attempt to draw quantitative conclusions as to the quantum state fidelity. However, one can find evidence in spectroscopy of the two-mode cat state (Fig. S12) that the magnitude of joint parity is indeed higher than 0.9.

M. Bell's Inequality

The two-mode cat state is a quantum mechanical system consisting of two continuous-variable subsystems. For two continuous-variable systems, the correlation between their individual parities after independent displacements has a classical upper bound, which can be described by a CHSH-type Bell's inequality using the formulation proposed in Ref. 21 and discussed in Ref. 22. Arbitrarily choosing two test displacements β_A, β'_A in Alice and two test displacements β_B, β'_B in Bob, the Bell signal $\mathcal{B}$ can be constructed from parity correlations after all four combinations of displacements in the two cavities:

$$\mathcal{B} = \big|\langle P_A(\beta_A)P_B(\beta_B)\rangle + \langle P_A(\beta'_A)P_B(\beta_B)\rangle + \langle P_A(\beta_A)P_B(\beta'_B)\rangle - \langle P_A(\beta'_A)P_B(\beta'_B)\rangle\big| \leq 2 \quad \text{(S24)}$$

where $P_i(\beta) \equiv D_{\beta_i} P_i D_{\beta_i}^\dagger$ (i =A, B) is the displaced parity operator. Here measuring parity after different displacements is analogous to measuring σ_z of a spin-$\frac{1}{2}$ system after
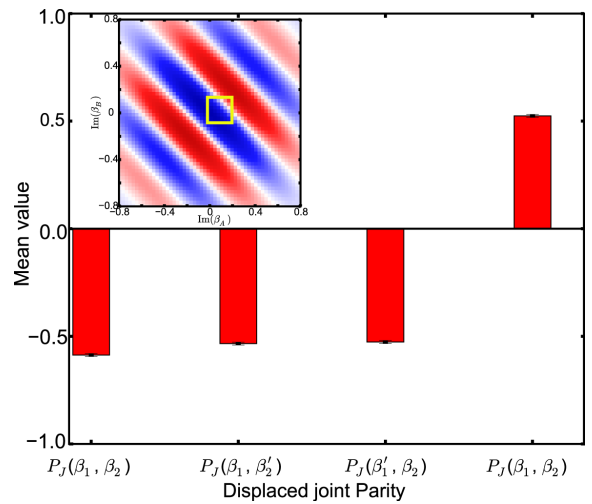

FIG. S16. **Bell signal of an odd two-mode cat state.** Red bars show the amplitude of scaled joint Wigner function at the selected sampling points in the phase space defined by the imaginary amplitudes of β_A, β_B. Inset shows the location of the chosen sampling points in phase space

different rotations.

Equivalently, this Bell signal is represented by the values of joint Wigner function (or displaced joint parity) at the four vertices of a rectangle:

$$\mathcal{B} = \frac{\pi^2}{4}\big|W_J(\beta_A, \beta_B) + W_J(\beta'_A, \beta_B) + W_J(\beta_A, \beta'_B) - W_J(\beta'_A, \beta'_B)\big| \leq 2 \quad \text{(S25)}$$

For a quantum state with entanglement between the two subsystems, this Bell's inequality can be violated. For near-optimal violation, we choose a square in the $\text{Im}(\beta_A)$-$\text{Im}(\beta_B)$ plane with prominent interference fringes. The square is positioned to have three of the vertices close to the minimum of the central negative fringe and one in the vicinity of the maximum of the adjacent positive fringe, using $\beta_A = \beta_B = -i\pi/(16\beta) = -0.102$ and $\beta'_A = \beta'_B = 3i\pi/(16\beta) = 0.307$ (Fig. S16). Given these sampling points, the measured amplitude gives a Bell signal $\mathcal{B} = 2.17 \pm 0.01$, surpassing the classical threshold by more than 10 standard deviations. This indicates the non-classical nature of the two-mode cat state and the presence of quantum correlations between the two modes. This also demonstrates the robustness of our experimental technique in both the

creation of the quantum mechanical two-mode cat state as well as the joint parity measurement procedure.

N. Encoded Two-qubit Tomography

Complete joint-Wigner tomography of the two-cavity quantum state requires large numbers of measurements. However, if we are restricted to a particular coherent state basis of the two cavities to encode two logical qubits (as described in the main text), efficient Pauli tomography can be performed for this logical subspace with a total of only 16 measurements.

Using the encoding scheme $|\alpha\rangle_i \to |0\rangle_j$ and $|-\alpha\rangle_j \to |1\rangle_i$ (i, j= A or B), the single-qubit Pauli operators are:

$$
\begin{aligned}
X_j &= |-\alpha\rangle_j\langle\alpha|_j + |\alpha\rangle_j\langle-\alpha|_j \\
Y_j &= i|-\alpha\rangle_j\langle\alpha|_j - j|\alpha\rangle_j\langle-\alpha|_j \\
Z_j &= |\alpha\rangle_j\langle\alpha|_j - |-\alpha\rangle_j\langle-\alpha|_j \\
I_j &= |\alpha\rangle_j\langle\alpha|_j + |-\alpha\rangle_j\langle-\alpha|_j
\end{aligned} \tag{S26}
$$

Following the derivation in Ref. 23, these single-qubit operators can be linked to the displaced parity operators of a cavity $(P_j(\beta) \equiv D_{\beta_j} P_j D_{\beta_j}^\dagger)$:

$$
\begin{aligned}
X_j &\approx P_j(0) \\
Y_j &\approx P_j\left(\frac{j\pi}{8\alpha}\right) \\
Z_j &\approx P_j(\alpha) - P_j(-\alpha) \\
I_j &\approx P_j(\alpha) + P_j(-\alpha)
\end{aligned} \tag{S27}
$$

These relations can be verified by projecting the displaced parity operators onto the encoded subspace using the projector $M_j = |\alpha\rangle_j\langle\alpha|_j + |-\alpha\rangle_j\langle-\alpha|_j$ (for more details, see supplementary notes in Ref. 23).

The 16 two-qubit observables are products of single-qubit Pauli operators, and can all be expressed in the form of displaced joint parities. Since operators in different cavities commute,

$$
P_A(\beta_A)P_B(\beta_B) = D_{\beta_A} D_{\beta_B} P_J D_{\beta_A}^\dagger D_{\beta_B}^\dagger \equiv P_J(\beta_A, \beta_B) \tag{S28}
$$

we have,

$$
\begin{aligned}
I_A I_B &= P_J(\alpha,\alpha) + P_J(\alpha,-\alpha) + P_J(-\alpha,\alpha) + P_J(-\alpha,-\alpha) \\
I_A X_B &= P_J(\alpha,0) + P_J(-\alpha,0) \\
I_A Y_B &= P_J\left(\alpha, \frac{i\pi}{8\alpha}\right) + P_J\left(-\alpha, \frac{i\pi}{8\alpha}\right) \\
I_A Z_B &= P_J(\alpha,\alpha) - P_J(\alpha,-\alpha) + P_J(-\alpha,\alpha) - P_J(-\alpha,-\alpha) \\
X_A I_B &= P_J(0,\alpha,) + P_J(0,-\alpha) \\
Y_A I_B &= P_J\left(\frac{i\pi}{8\alpha},\alpha\right) + P_J\left(\frac{i\pi}{8\alpha},-\alpha\right) \\
Z_A I_B &= P_J(\alpha,\alpha) + P_J(\alpha,-\alpha) - P_J(-\alpha,\alpha) - P_J(-\alpha,-\alpha) \\
X_A X_B &= P_J(0,0) \\
X_A Y_B &= P_J\left(0, \frac{i\pi}{8\alpha}\right) \\
X_A Z_B &= P_J(0,\alpha) - P_J(0,-\alpha) \\
Y_A X_B &= P_J\left(\frac{i\pi}{8\alpha},0\right) \\
Y_A Y_B &= P_J\left(\frac{i\pi}{8\alpha}, \frac{i\pi}{8\alpha}\right) \\
Y_A Z_B &= P_J\left(\frac{i\pi}{8\alpha},\alpha\right) - P_J\left(\frac{i\pi}{8\alpha},-\alpha\right) \\
Z_A X_B &= P_J(\alpha,0) - P_J(-\alpha,0) \\
Z_A Y_B &= P_J\left(\alpha, \frac{i\pi}{8\alpha}\right) - P_J\left(-\alpha, \frac{i\pi}{8\alpha}\right) \\
Z_A Z_B &= P_J(\alpha,\alpha) - P_J(\alpha,-\alpha) - P_J(-\alpha,\alpha) + P_J(-\alpha,-\alpha)
\end{aligned} \tag{S29}
$$

To obtain a full set of two-qubit tomography measurements, we perform joint parity measurements following 16 different cavity displacement combinations ($\beta = 0$, $\frac{i\pi}{8\alpha}$, α and $-\alpha$ in each cavity), and the 16 two-qubit Pauli operators can be computed from Eq. (S29).

[1] M. Reagor, W. Pfaff, C. Axline, R. W. Heeres, N. Ofek, K. Sliwa, E. Holland, C. Wang, J. Blumoff, K. Chou, M. J. Hatridge, L. Frunzio, M. H. Devoret, L. Jiang, and R. J. Schoelkopf, arXiv:1508.05882 [cond-mat, physics:quant-ph] (2015).

[2] M. Reagor, H. Paik, G. Catelani, L. Sun, C. Axline, E. Holland, I. M. Pop, N. A. Masluk, T. Brecht, L. Frunzio, M. H. Devoret, L. Glazman, and R. J. Schoelkopf, Applied Physics Letters 102, 192604 (2013).

[3] C. Axline, M. Reagor, P. Reinhold, R. Heeres, C. Wang, W. Pfaff, Y. Chu, L. Frunzio, and R. Schoelkopf, In preparation (2016).

[4] S. E. Nigg, H. Paik, B. Vlastakis, G. Kirchmair, S. Shankar, L. Frunzio, M. H. Devoret, R. J. Schoelkopf, and S. M. Girvin, Physical Review Letters 108, 240502 (2012).

[5] G. Kirchmair, B. Vlastakis, Z. Leghtas, S. E. Nigg, H. Paik, E. Ginossar, M. Mirrahimi, L. Frunzio, S. M. Girvin, and R. J. Schoelkopf, Nature 495, 205 (2013).

[6] A. Wallraff, D. I. Schuster, A. Blais, L. Frunzio, R.-S. Huang, J. Majer, S. Kumar, S. M. Girvin, and R. J. Schoelkopf, Nature 431, 162 (2004).

[7] Z. Leghtas, T. Touzard, A. Petrenko, I. Pop, A. Kou, B. Vlastakis, A. Narla, K. Sliwa, S. Shankar, M. Hatridge, V. Albert, L. Jiang, L. Frunzio, R. Schoelkopf, M. Mirrahimi, and M. Devoret, In preparation (2016).

[8] M. J. Peterer, S. J. Bader, X. Jin, F. Yan, A. Kamal, T. J. Gudmundsen, P. J. Leek, T. P. Orlando, W. D. Oliver, and S. Gustavsson, Physical Review Letters 114, 010501 (2015).

[9] R. W. Heeres, B. Vlastakis, E. Holland, S. Krastanov, V. V. Albert, L. Frunzio, L. Jiang, and R. J. Schoelkopf, Physical Review Letters 115, 137002 (2015).

[10] B. Vlastakis, G. Kirchmair, Z. Leghtas, S. E. Nigg, L. Frunzio, S. M. Girvin, M. Mirrahimi, M. H. Devoret, and R. J. Schoelkopf, Science 342, 607 (2013).

[11] Z. Leghtas, G. Kirchmair, B. Vlastakis, M. H. Devoret, R. J. Schoelkopf, and M. Mirrahimi, Physical Review A 87, 042315 (2013).

[12] I. Chuang, D. W. Leung, and Y. Yamamoto, Physical Review A 56 (1997).

[13] M. Michael, M. Silveri, R. Brierley, V. V. Albert, J. Salmile-

hto, L. Jiang, and S. M. Girvin, In preparation (2016).

[14] L. Sun, A. Petrenko, Z. Leghtas, B. Vlastakis, G. Kirchmair, K. M. Sliwa, A. Narla, M. Hatridge, S. Shankar, J. Blumoff, L. Frunzio, M. Mirrahimi, M. H. Devoret, and R. J. Schoelkopf, Nature **511**, 444 (2014).

[15] N. Khaneja, T. Reiss, C. Kehlet, T. Schulte-Herbrggen, and S. J. Glaser, Journal of Magnetic Resonance **172**, 296 (2005).

[16] U. Leonhardt, *Measuring the Quantum State of Light* (Cambridge University Press, 1997).

[17] C. Rigetti, J. M. Gambetta, S. Poletto, B. L. T. Plourde, J. M. Chow, A. D. Crcoles, J. A. Smolin, S. T. Merkel, J. R. Rozen, G. A. Keefe, M. B. Rothwell, M. B. Ketchen, and M. Steffen, Physical Review B **86**, 100506 (2012).

[18] M. Mirrahimi, Z. Leghtas, V. V. Albert, S. Touzard, R. J. Schoelkopf, L. Jiang, and M. H. Devoret, New Journal of Physics **16**, 045014 (2014).

[19] F. Motzoi, J. M. Gambetta, P. Rebentrost, and F. K. Wilhelm, Physical Review Letters **103**, 110501 (2009).

[20] Z. Chen, J. Kelly, C. Quintana, R. Barends, B. Campbell, Y. Chen, B. Chiaro, A. Dunsworth, A. Fowler, E. Lucero, E. Jeffrey, A. Megrant, J. Mutus, M. Neeley, C. Neill, P. OMalley, P. Roushan, D. Sank, A. Vainsencher, J. Wenner, T. White, A. Korotkov, and J. M. Martinis, Physical Review Letters **116**, 020501 (2016).

[21] K. Banaszek and K. Wdkiewicz, Physical Review Letters **82**, 2009 (1999).

[22] P. Milman, A. Auffeves, F. Yamaguchi, M. Brune, J. M. Raimond, and S. Haroche, The European Physical Journal D - Atomic, Molecular, Optical and Plasma Physics **32**, 233 (2005).

[23] B. Vlastakis, A. Petrenko, N. Ofek, L. Sun, Z. Leghtas, K. Sliwa, Y. Liu, M. Hatridge, J. Blumoff, L. Frunzio, M. Mirrahimi, L. Jiang, M. H. Devoret, and R. J. Schoelkopf, Nature Communications **6**, 8970 (2015).